REVIEW ARTICLE

Applications of graphitic carbon nitride-based S-scheme heterojunctions for environmental remediation and energy conversion

Article history:
Received: 30-11-2022
Revised: 10-01-2023
Accepted: 16-01-2023

Anita Sudhaik[a], Sonu[b], Vasudha Hasija[c], Rangabhashiyam Selvasembian[d], Tansir Ahamad[e], Arachana Singh[f], Aftab Aslam Parwaz Khan[g], Pankaj Raizada[h], Pardeep Sing[i]

Abstract: The contemporary era's top environmental problems include the lack of energy, recycling of waste resources, and water pollution. Due to the speedy growth of modern industrialization, the utilization of non-renewable sources has increased rapidly, which has caused many serious environmental and energy issues. In photocatalysis, as a proficient candidate, g-C_3N_4 (metal-free polymeric photocatalyst) has gained much attention due to its auspicious properties and excellent photocatalytic performance. But, regrettably, the quick recombination of photoinduced charge carriers, feeble redox ability, and inadequate visible light absorption are some major drawbacks of g-C_3N_4 that hamper its photocatalytic ability. Henceforth, these significant limitations can be solved by incorporating modification strategies. Among all modification techniques, the amalgamation of g-C_3N_4 with two or more photocatalytic semiconducting materials via heterojunction formation is more advantageous. In this review, we have discussed various modification strategies, including conventional, Z-scheme and S-scheme heterojunctions. S-scheme heterojunction is consideredan efficient and profitable charge transferal pathway due to the excellent departure and transferal of photoexcited charge carriers with outstanding redox ability. Consequently, the current review is focused on various photocatalytic applications of S-scheme-based g-C_3N_4 photocatalysts in pollutant degradation, H_2 production, and CO_2 reduction.

Keywords: g-C_3N_4; Modification strategies; S-scheme heterojunction; Pollutants degradation; Energy conversion.

[a] School of Advanced Chemical Sciences, Faculty of Basic Sciences, Shoolini University, Solan (HP), India-173229.
[b] School of Advanced Chemical Sciences, Faculty of Basic Sciences, Shoolini University, Solan (HP), India-173229.
[c] School of Advanced Chemical Sciences, Faculty of Basic Sciences, Shoolini University, Solan (HP), India-173229.
[d] Department of Biotechnology, School of Chemical and Biotechnology, SASTRA Deemed University, Thanjavur 613401, Tamilnadu, India.
[e] Department of Chemistry, College of Science, King Saud University, Riyadh 11451, Saudi Arabia.
[f] Advanced Materials and Processes Research Institute, Hoshangabad Road, Bhopal (MP), India. 462026.
[g] Center of Excellence for Advanced Materials Research, King Abdulaziz University, P.O. Box 80203, Jeddah, 21589, Saudi Arabia.
[h] School of Advanced Chemical Sciences, Faculty of Basic Sciences, Shoolini University, Solan (HP), India-173229.
[i] School of Advanced Chemical Sciences, Faculty of Basic Sciences, Shoolini University, Solan (HP), India-173229. Corresponding author: pardeepchem@gmail.com

List of Abbreviations

Acetylene black (AB); All-solid-state (ASS); Apparent quantum efficiency (AQE); Bisphenol A (BPA); Carbon nitride quantum dots (CNQDs); Cefixime (CFX); Ciprofloxacin (CIP); Conduction band (Vedula *et al.*); Diclofenac (DCF); Electron-hole pairs (EHPs); Electrochemical impedance spectroscopy (EIS); Electron proton resonance (EPR); Fluoroquinolones (FQs); Graphene oxide (GO); Levofloxacin (LVF); Internal electric field (IEF); Methyl orange (MO); Methylene blue (MB); Nanorods (NRs); Nanosheets (NSs); Nanotubes (NT); Near-infrared (NIR); NPs (nanoparticles); Norfloxacin (NOR); Photocatalytic water splitting (PWS); Photoluminescence (González-Pleiter *et al.*); Reactive oxygen species (ROS); Rhodamine B (RhB); Specific surface area (SSA); Surface plasmon resonance (SPR); Tetracycline (TC); Valence band (VB)

Highlights

- An overview of g-C_3N_4 as a photocatalyst.
- Modification strategies of g-C_3N_4 photocatalysts are explored with their mechanisms.
- S-scheme-based g-C_3N_4 heterojunctions were elaborated for pollutant degradation.
- S-scheme-based g-C_3N_4 heterojunctions in energy conversion are explored
- Current challenges with some future perspectives are explained.

1. INTRODUCTION

Recently, viable photocatalytic clean energy production has been well-thought-out as an efficient and advantageous solution to minimize the energy shortage and environmental pollution crisis. The rise in living standards and growing population are the primary reason for the depletion of non-renewable energy sources due to their excessive use. Approximately 80% of global energy utilization includes non-renewable fossil fuels (Akhundi *et al.*, 2020; Akhundi *et al.*, 2019; Amin *et al.*, 2022). Several kinds of pharmaceuticals, textiles, leather, food products and paper mills industries discharge various harmful pollutants into water sources that are deprived of any treatment processes (Lellis *et al.*, 2019; Patel *et al.*, 2019; Sasi *et al.*, 2020; Yang *et al.*, 2021). Consequently, energy deficit and environmental pollution are major concerns in the current era. Due to companies' excessive growth, wastewater contains agriculture-based chemicals, medicines, personal care products, and industrial chemicals as pollutants (Freeman *et al.*, 1992; Sharma *et al.*, 2017; Thornton *et al.*, 2002). Conventionally, many physical, chemical, and biological methods have been used to resolve these issues, but unfortunately, these techniques have poor pollutant removal efficiency (Cervantes-Avilés *et al.*, 2021; Crini *et al.*, 2019; Gupta *et al.*, 2021). Henceforth, photocatalytic waste water treatment, an advanced oxidation process, has gained much consideration due to its eco-friendly features (Bie *et al.*, 2021b). Photocatalysis technology has been extensively utilized for various energy and environmental applications (Akhundi *et al.*, 2022; Hou *et al.*, 2020), such as H_2O splitting, H_2O_2 production, CO_2/N_2 reduction, O_2 evolution, gas purification, pollutants degradation, (Bai *et al.*, 2022; Chen, *et al.*, 2021; Kudo *et al.*, 1998; Liu, *et al.*, 2021; Niu *et al.*, 2021; Sudhaik *et al.*, 2022; Xu, *et al.*, 2021) etc. Photocatalytic oxidation a smart pathway, has more advantages for environmental pollutants removal.

In photocatalysis production of highly reactive oxygen species (ROS), i.e. $^{\bullet}O_2^-$ and $^{\bullet}OH$ radicals, take place by the photoinduced charge carriers (e^- and h^+) in the presence of solar or other light sources (Ameta *et al.*, 2018; Sabri *et al.*, 2021; Serpone, 2000). The most commonly employed semiconductors in photocatalysis are TiO_2, ZnO, g-C_3N_4, BiOCl, Ag_3VO_4, Fe_2O_3, etc. (Chen *et al.*, 2010; Gu *et al.*, 2016; Guo *et al.*, 2019; Hu *et al.*, 2007; Mishra *et al.*, 2015; Sudhaik *et al.*, 2022). Some of the extensively utilized wide band gap photocatalysts (TiO_2, ZnO, etc.) have certain limitations and only respond to UV light which diminishes solar energy utilization and significantly limits their practical applications (Sabri *et al.*, 2021; Wang *et al.*, 2012; Xu *et al.*, 2012). Consequently, visible-light-responsive photocatalysts with tremendous photocatalytic ability grabbed the attention of researchers and have been employed for various photocatalytic applications (Kumar *et al.*, 2018; Pirhashemi *et al.*, 2018; Xiao *et al.*, 2020; Zhou *et al.*, 2021). The photo-oxidation caused by visible light is more promising as visible light is easily accessible, harmless for living organisms and contains ~45% part of solar irradiation (Brillas *et al.*, 2015; Reddy *et al.*, 2016; Wang *et al.*, 2016). In this context, numerous visible-light-responsive photocatalysts, *viz.* Bi_2O_3, $BiVO_4$, WO_3, CdS, MoS_2, g-C_3N_4, etc., have been synthesized for numerous photocatalytic applications (Cheng *et al.*, 2018; Li *et al.*, 2018; Nguyen *et al.*, 2020; Niu *et al.*, 2013; Sudhaik *et al.*, 2020; Tahir *et al.*, 2017). Amongst all visible light-driven photocatalysts, graphite-like carbon nitride (g-C_3N_4), a typical metal-free photocatalyst, has attained the consideration of the researchers owing to apt energy gap (2.7 eV), non-toxicity, cost-effectiveness, exceptional electronic properties, excellent thermal stability, simply synthesis at large-scale and high reduction ability (Fu *et al.*, 2018; Liu *et al.*, 2021; Wen *et al.*, 2017). It is a promising photocatalyst with a 2D layered framework already prepared since 2009 for H_2 production due to its outstanding properties (Chen *et al.*, 2009; Wang *et al.*, 2009; Yan *et al.*, 2009). Instead of the abovementioned exceptional properties, some drawbacks like smaller specific surface area (SSA), poorly visible light harnessing and fast charge carriers recombination constrained its photoactivity (Xiao *et al.*, 2020; Zhou *et al.*, 2021).

Therefore, to minimize theses drawbacks and to boost the photoactivity, a multitude of modification strategies have been utilized, for example, morphology control, cocatalyst loading, metallic and non-metallic doping, and heterojunction formation and use of support materials (Cheng *et al.*, 2021; Fu *et al.*, 2018; Li *et al.*, 2021; Wen *et al.*, 2017; Zhu *et al.*, 2021), etc.

In the midst of all modification strategies, heterojunction construction is one of the utmost efficient ways to prolong visible light garnering and to reduce the photocarriers recombination via escalating photocarriers separation and migration (Meng *et al.*, 2019; Wang *et al.*, 2014). Heterojunction techniques include conventional, Z-scheme and S-scheme (step-scheme) heterojunction, which have been employed to enhance the photo-oxidation ability of single photocatalyst through effective photocarriers separation as a result, promoting H_2 production or pollutants degradation efficiency (Kumar *et al.*, 2021; Wang *et al.*, 2020). Numerous reports were published on traditional type-II heterojunctions of g-C_3N_4 with other semiconductors, e.g. ZnO, $ZnFe_2O_4$, $BiPO_4$ and CdS, etc. (Borthakur *et al.*, 2019; He *et al.*, 2015; Xu *et al.*, 2017; Zhu *et al.*, 2021). Photocarrier transfer process in type-II heterojunction is considered perfect due to charge carriers split-up. Still, thermodynamically type-II is imperfect due to significant electrostatic repulsion among e^- and h^+, which prevents their transferal in type-II heterojunction (Li *et al.*, 2022; Xu *et al.*, 2020). Because of type-II heterostructures limitations, traditional Z-Scheme heterojunction was offered to speed-up charge carriers separation rate while preserving great redox ability, but this fit only for the solution systems (Wu *et al.*, 2022; Zhou *et al.*, 2014). Later on, researchers suggested all-solid-state (ASS) and direct Z-scheme heterojunctions with enhanced features (Li *et al.*, 2021; Low *et al.*, 2017a). Still, both these types of heterojunctions have several faults and conflicts. Therefore, to diminish the flaws of type-II and Z-Scheme heterojunctions, a novel kind of S-scheme heterojunction was recommended by Yu and his research team first time (Cheng *et al.*, 2021; Fu *et al.*, 2019; Xu *et al.*, 2020).

In S-scheme heterojunctions, two types of semiconductor photocatalysts are required, i.e. oxidative photocatalysts and reductive photocatalysts, which can be referred to as denoted by SC-I and SC-II, respectively (Wang *et al.*, 2022). In this heterostructure photocatalytic system, the e^- and h^+ are retained individually in the SC-IICB and in SC-IVB, and the migration of e^- followed the path like a "step" (Kumar *et al.*, 2021; Zhang *et al.*, 2022). Similarly, in this charge transfer pathway, the fragile redox e^- and h^+ are used and transported even though resilient ones are reserved and instigated for further photocatalytic reactions and, thus, promote the redox ability of the heterostructure (Bao *et al.*, 2021; Wang *et al.*, 2021; Xu *et al.*, 2020). In this photocatalytic system, comparatively unused h^+ of semiconductor with higher valance band (VB) potential and unused e^- of semiconductor with lower conduction band (Vedula *et al.*, 2013) potential are united and abolished at the interface (Vedula *et al.*, 2013). So far, several reports have been published on S-scheme based g-C_3N_4 heterojunction systems for energy conversion and pollutant degradation. For instance, 2D/2D Bi_2MoO_6/g-C_3N_4, S-scheme heterostructure with extended visible-light absorption via Au loading was prepared to employ a photoreduction and hydrothermal method by Li and coworkers (Li *et al.*, 2020). The synthesized S-scheme Bi_2MoO_6/g-C_3N_4/Au nanocomposite was used to remove Rhodamine B (RhB) dye. The degradation results confirmed that Bi_2MoO_6/g-C_3N_4/Au nanocomposite had almost 9.7 and 13.1 folds higher RhB removal efficacy than the Bi_2MoO_6 and g-C_3N_4 single photocatalysts, respectively. Au nanoparticles (NPs) acted as a co-catalyst to boost e^- relocation and departure rate from CB of g-C_3N_4. Li and his research team reported the preparation of visible light-assisted S-scheme-based porous g-C_3N_4/TiO_2 photocatalyst for H_2 generation and RhB degradation (Li, B. *et al.*, 2021). The observed H_2 production rate and RhB removal efficiency of optimized 40-MTO/PCN were 2137.3 μmol $h^{-1}g^{-1}$ and 35.24%, respectively. Similarly, CO_2 photocatalytic reduction and Bisphenol-S degradation were reported by Die *et al.* using g-C_3N_4/Cu_2O@Cu S-scheme photocatalyst (Dai *et al.*, 2022b). The study explored the highest CO and CH_4 production rate for S-scheme g-C_3N_4/Cu_2O@Cu-4 nanocomposite, i.e. 13.5 (10.8 μmol $h^{-1}g^{-1}$) and 15.5 folds (3.1 μmol $h^{-1}g^{-1}$) greater than bare Cu_2O, respectively. Also, g-C_3N_4/Cu_2O S-scheme heterojunction had shown 49.5% Bisphenol-S degradation than bare Cu_2O (24.8%) and g-C_3N_4 (31.4%) within 120 min of photocatalytic reaction. In the discussed work, the enhanced efficiency was due to S-scheme charge transfer pathway that efficiently enhanced separation and transferal of photoexcited charge carriers with outstanding redox ability.

Henceforth, a new and efficient S-scheme heterojunction with exceptional assistances, such as a solid capability to boost photoexcited charge carriers split-up and concurrent retaining of the inclusive/higher redox potential of photocatalyst (Xu *et al.*, 2020), has made the current research community to focus more towards S-scheme based photocatalytic system. Thus, knowing the advantageous of g-C_3N_4 photocatalyst and S-scheme heterojunction (as modification strategy), the current review article is based on S-scheme heterojunctions of g-C_3N_4. To date, limited reviews have been published on S-scheme-based g-C_3N_4 (Li *et al.*, 2022). So, in this review, we have summarized different modification strategies (traditional, Z-scheme and S-scheme heterojunction) to boost the photocatalytic ability of a single g-C_3N_4 photocatalyst. Similarly, due to aforesaid benefits of the S-scheme charge transfer route, we have broadly discussed the diverse photocatalytic applications of S-scheme based g-C_3N_4 heterojunctions for the removal of various water contaminants (Antibiotics, textile dyes, phenols, Cr(VI) reduction), photocatalytic H_2 production, CO_2 photo-reduction into fuels from newly published works. In conclusion, based on recent research progress, we have also proposed some current challenges and key points associated with the future leaning in their construction/synthesis and applications of S-scheme based g-C_3N_4 heterostructures, which can be helpful for further innovative research (Li *et al.*, 2022).

2. g-C_3N_4 PHOTOCATALYST WITH ITS MODIFICATION STRATEGIES

In general, g-C_3N_4 is an n-type semiconductor with an energy gap of 2.7 eV that harvest visible light, making it a visible light-driven semiconductor material (Dai *et al.*, 2021; Sudhaik *et al.*, 2020; Wang *et al.*, 2009). The g-C_3N_4 has numerous exceptional properties like non-toxicity, stability, low-cost, appropriate energy-gap, and visible-light absorption. But, still, pristine g-C_3N_4 has some glitches like low quantum yield, charge recombination, poor conductivity, etc. therefore, it is modified every so often (Akhundi *et al.*, 2019; Cao *et al.*, 2015; Li *et al.*, 2021; Wang *et al.*, 2014). g-C_3N_4 can be fabricated by a simple preparation route i.e. the thermal polycondensation/thermal polymerization of melamine or dicyandiamide precursor. It can also be prepared using thermal-polymerization of urea (Akhundi *et al.*, 2020; Alwin *et al.*, 2020a; Alwin *et al.*, 2020b; Yang *et al.*, 2021). Though the procedure is simple, during thermal polycondensation of melamine or dicyandiamide, some toxic gases are released which can pollute the atmosphere. However in the case of thermal polymerization of urea, the attained yield is meager, and the calcination environment, as well as the temperature, are stringent (Wu *et al.*, 2022). The expected photocatalytic mechanism of g-C_3N_4 photocatalyst is presented in Fig.1a, indicating the photocatalytic process in different steps, such as excitation of electrons in the presence of light to form photoexcited charge carriers (electrons and holes), charge carrier's migration towards the surface and finally the participation of charge carriers in further redox reactions on g-C_3N_4 photocatalyst surface to produce ROS (Bie *et al.*, 2021a; Li *et al.*, 2022; Sudhaik *et al.*, 2022). Although due to constricted bandgap, g-C_3N_4 utilize visible light and generates $^{\bullet}O_2^-$ radicals in its CB but still can't produce $^{\bullet}OH$ radicals (Sudhaik *et al.*, 2020; Wei *et al.*, 2021). As in photocatalysis, more –ve CB potential and +ve VB potential are essential to boost the surface redox reactions. Hence, it is challenging for a bare photocatalyst to exhibit a lower energy gap and strong redox capabilities concurrently (Li *et al.*, 2016; Li, Yang *et al.*, 2020; Wang *et al.*, 2021). Furthermore, the attainment of efficient charge carriers' separation is also an excellent challenge for a single g-C_3N_4 photocatalyst. Despite good and exceptional possessions, g-C_3N_4 has several drawbacks as a photocatalyst (Cao *et al.*, 2015; Liao *et al.*, 2019; Yang *et al.*, 2021; Yuan *et al.*, 2022). To minimize those limitations and to augment the photocatalytic ability of g-C_3N_4 with extended visible light absorption, various modification strategies have been adopted such as metal/nonmetal elements doping, heterojunctions formation, coupling with support materials (combination of two or more semiconductors) (Diao *et al.*, 2021; Li *et al.*, 2022; Li *et al.*, 2020; Zhang *et al.*, 2021), etc. These modification strategies not only enrich the light-harvesting but also improve the photodegradation ability of g-C_3N_4 photocatalysts in different fields, and some of the examples have been discussed in the next section.

2.1. Modification strategies

To date numerous modification strategies have been employed towards g-C_3N_4 photocatalyst to improve its photocatalytic properties, but amongst all strategy, construction of heterojunction of g-C_3N_4

photocatalyst with different semiconducting materials helps to achieve all the mentioned concerns at the same time (Lian *et al.*, 2021; Wang *et al.*, 2021; Wang *et al.*, 2021; Zhu *et al.*, 2021). To date, numerous g-C_3N_4-based heterojunctions have been synthesized and have been used for various photocatalytic applications such as type-II, Schottky, Z-scheme and p-n heterojunction (Huang *et al.*, 2019; Li *et al.*, 2020; Maihemllti *et al.*, 2021; Ren *et al.*, 2019; Wang *et al.*, 2021; Yang *et al.*, 2019). From these heterojunctions, Z-scheme, S-scheme, and type-II heterojunctions comprising two n- and p-type SCs have gained much consideration (Xu *et al.*, 2020; Zhang *et al.*, 2020).

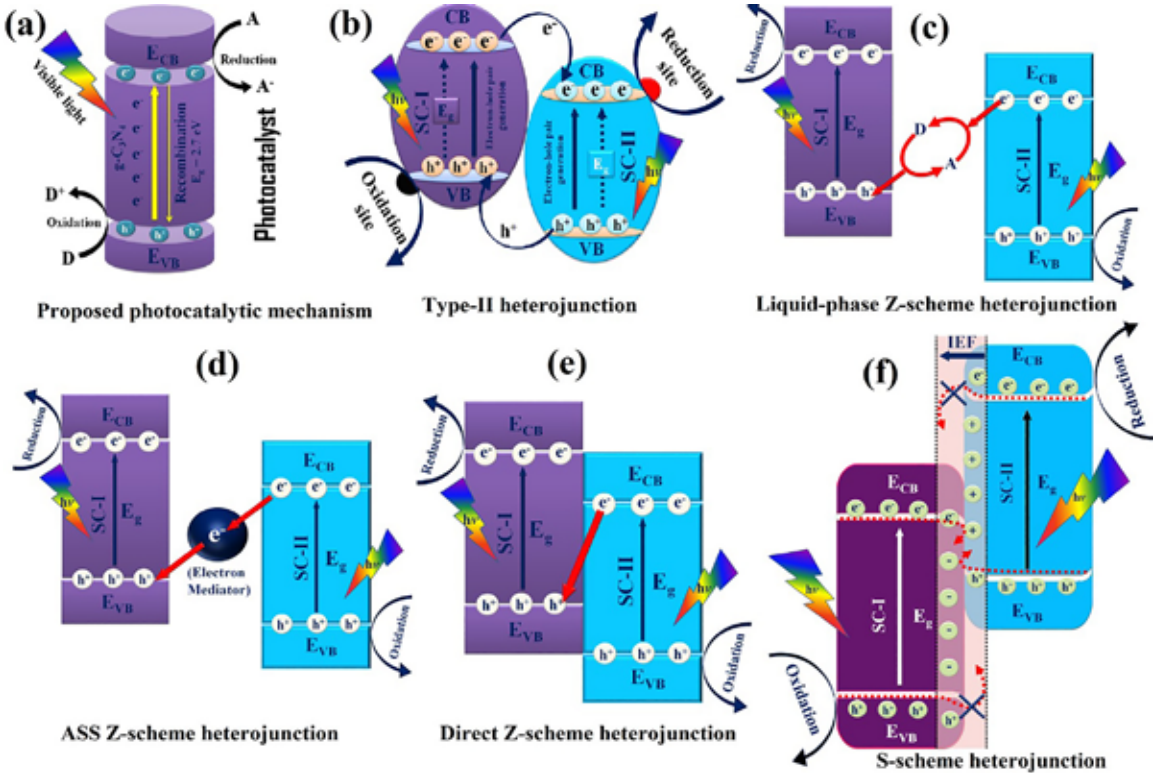

Figure 1. (a) The proposed photocatalytic mechanism of g-C_3N_4 photocatalyst, Charge transferal route in various types of heterojunctions: (b) Type-II, (c-e) Z-scheme, ((c) Liquid-phase, (d) ASS and (e) Direct Z-scheme heterojunctions), and (f) S-scheme heterojunctions, Reprinted with permission from Elsevier (License No. 5431430538676) (Kumar *et al.*, 2021)

2.1.1. Conventional Heterojunctions

Conventional heterostructures include p-n heterojunctions and Schottky junctions, as well as type-I, type-II, and type-III heterostructures (Kumari *et al.*, 2022; Low *et al.*, 2017b). In type-I heterojunction, photoinduced CB e^- and VB h^+ present in the semiconductor-I (SC-I) migrate to the VB and CB of semiconductor-II (SC-II), respectively. All the charge carriers were stored in SC-II; hence due to no progress in charge carriers separation in this heterojunction, its photocatalytic activity is low. In type-II heterojunction, CB e^- migrates from SC-I to CB of SC-II, and h^+ transfers from VB of SC-II to SC-I. The remaining photoinduced h^+ in VB of SC-I and e^- in CB of SC-II, respectively, take part in the further redox processes. Therefore, strong redox capability and spatially dispersed redox reaction sites are possible because of the type-II charge-transfer mechanism (Fig. 1b) (Liu *et al.*, 2020; Wang *et al.*, 2013). Sun and coworkers designed g-C_3N_4/ZnO composites with type-II heterojunction for photocatalytic efficiency of p-nitrophenol and MO (Sun *et al.*, 2012). The g-C_3N_4/ZnO nanocomposites were more photocatalytic than pristine g-C_3N_4 and ZnO. Photoexcited e^- in the CB of g-C_3N_4 can reduce O_2 to produce highly oxidizing $^{\bullet}O_2^-$. However, photoexcited h^+ in the VB of ZnO can directly oxidize MO. The increased photocatalytic performance was demonstrated by

suppression of e^{-}-h^{+} recombination and the production of more $^{\bullet}O_2^{-}$, showing the boosted efficiency of g-C_3N_4/ZnO. Whereas the ideal type-II heterojunction may be able to segregate charge couples spatially, the increased e^{-}-h^{+} separation across the type-II heterojunction is insufficient to counteract the quick recombination of e^{-}-h^{+} that occurs on the semiconductor (Li *et al.*, 2022). To improve photocatalytic efficiency, it is proposed to design a photocatalyst with p-n heterojunction, which uses an extra electric field to speed up the photocarrier separation and relocation. The desirable photocatalyst with p-n heterojunction is fabricated using p-type and n-type SCs (Sah *et al.*, 1957; Wang *et al.*, 2019). The Fermi level of p-type SC is close to the VB, whereas that of n-type SC is close to the CB. Accordingly, an electric field is generated between two SC of different types. Photoexcited e^{-}-h^{+} pairs will dissociate under the influence of an electric field. Generally, because of its structural NH/NH_2 groups, which act as electron donors, g-C_3N_4 is classified as an n-type SC (Fu *et al.*, 2018). Cai *et al.* used in situ synthesis to construct a g-C_3N_4/CuS p-n heterostructures composite for the photodegradation of RhB and MB dye (Cai *et al.*, 2017). The photodegradation ability of the g-C_3N_4/CuS heterojunctions was significantly improved than bare CuS and g-C_3N_4. As presented in Fig. 2a, g-C_3N_4/CuS-2 nanocomposite had shown 96.8% RhB degradation efficacy within 60 min of light irradiation. CuS have more positive VB than g-C_3N_4, and g-C_3N_4 have more negative CB than CuS. So, photoexcited h^{+} readily transferred from VB of CuS to VB of g-C_3N_4, and photoinduced e^{-} quickly moved from CB of g-C_3N_4 to CB of CuS (Fig. 2b). A p-n heterostructure amid CuS and g-C_3N_4 allowed for the effectual separation of photo-induced charge carriers. Schottky junction is made up of an SC and a metal or metal-like substance, which is helpful in creating a spatial charge division area. Because of its distinctive properties, electrons may quickly jump from one material to another over the interface between them (Tung, 2001). The photocatalytic activity was enhanced because of the Fermi energy levels placement and considerable control of photocarrier recombination. Shen and coworkers fabricated g-C_3N_4-AB-CuS photocatalyst using acetylene black (AB) as the mediator that connected CuS and g-C_3N_4 photocatalysts to fabricate the highly stable ternary Schottky junction (Shen *et al.*, 2018). Incorporating AB nanoparticles into a g-C_3N_4 system resulted in the creation of Schottky junctions, so that the transport of e^{-} from CB of g-C_3N_4 to AB. Owing to the high electronic conductivity of AB, the recombination of photocarriers in g-C_3N_4-AB-CuS was reduced, proving the material's improved photocatalytic activity. Even though traditional type-II heterostructure appears to activate charge transmission, but it lowers the redox capability of charge carriers formed during photocatalytic system. Furthermore, the repulsion among the CB e^{-} and VB h^{+} of the two SCs hinder the transference of photocarriers in a type-II heterojunction (Li *et al.*, 2020; Liu *et al.*, 2021).

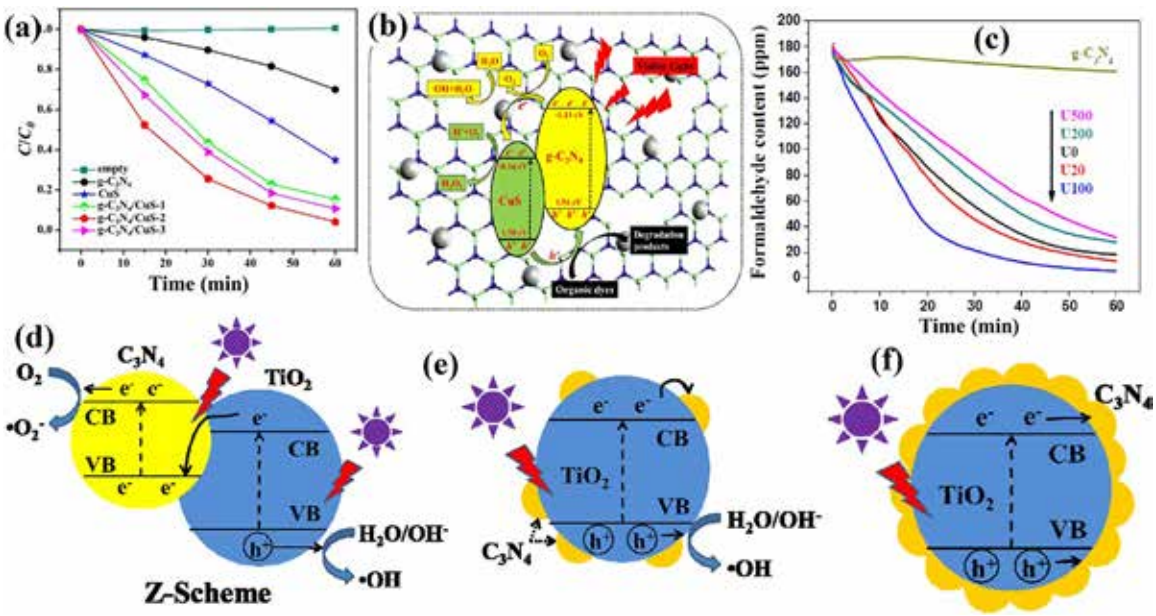

 https://doi.org/10.37819/nanofab.008.292

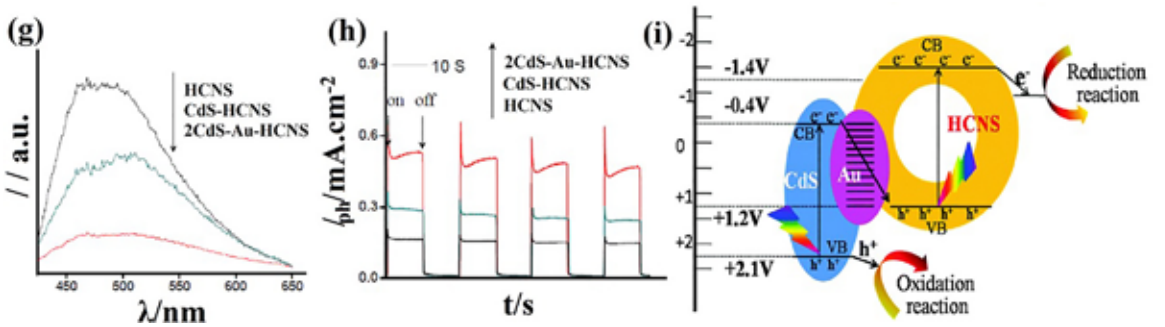

Figure 2. (a) RhB degradation rate beneath visible-light radiation (deprived of catalyst and using g-C_3N_4, CuS and g-C_3N_4/CuS photocatalysts) and (b) Representation of proposed RhB degradation mechanism using visible light assisted g-C_3N_4/CuS photocatalyst, Reprinted with permission from Elsevier (License No. 5433490423077) (Cai *et al.,* 2017). (g) PL spectra, (h) Photocurrent response, and (i) Proposed photocatalytic mechanism presenting Z-scheme electron transferal in CdS-Au-HCNS nanocomposite, Reprinted with permission from RSC (License ID. 1292693-2) (Yu *et al.,* 2013). (c) Assessment of the photoactivity of differently prepared samples for the decomposition of HCHO in air, (d) Graphic design showing photocarriers separation and transferal in Z-scheme g-C_3N_4/TiO_2 heterostructure beneath UV light exposure, Reprinted with permission from RSC (License ID. 1292693-1) (Zheng *et al.,* 2015).

2.1.2. Z-scheme Heterojunctions

All the heterojunctions above enhance e^--h^+ separation efficacy, but their redox ability is limited since oxidation and reduction processes happen on the semiconductor with lower oxidation and reduction potentials (Kumar *et al.*, 2021). To address these issues, leading researchers Bard *et al.* 1979 proposed developing a Z-scheme photocatalytic system (Bard *et al.*, 1979). In nature, green plants inspire this ideal transfer of charges since it's not only effectively separate photoinduced carriers but also provide strong and high redox proficiencies. Nonetheless, the redox mediators restrict the usefulness of Z-scheme photocatalytic systems to the liquid state (Fig. 1c). Therefore, the development of an ASS Z-scheme utilizing a metal as a mediator, or without a mediator, is expected (Fig. 1d). Yu and coworkers intended a potential mediator-free model in 2013 (Yu *et al.*, 2013). For recombination with photoinduced holes, photoexcited e^- on the lower-level CB of SC-II can go straight to the VB of SC-I. Direct Z-scheme mechanism defines this type of charge transferal (Fig. 1e). The g-C_3N_4-based metal sulfide nanohybrids have received multidisciplinary attention because of their broad ability in energy applications and their attribution to the improved photocatalytic Z-scheme system (Low *et al.*, 2017a). Starting with the traditional Z-scheme system to an electron mediator system and working our way up to the direct Z-scheme that doesn't need an electron mediator. ASS Z-scheme system has more significant applications in gas-solid and liquid-solid systems than their liquid-phase counterparts (Zhou *et al.*, 2014). Nanoparticles have been widely utilized as mediators in the building of Z-scheme because of their superior electrical conductivity. Another category of dual Z-scheme has also gained interest as it improves the photoactivity of a photocatalyst and minimizes the imitations of direct Z-scheme photocatalysts (Kumar *et al.*, 2021; Low *et al.*, 2017a). Considering these benefits, Yu and coworkers fabricate g-C_3N_4/TiO_2 direct Z-scheme heterojunction utilizing urea, P25 and TiO_2 as precursors in a one-step calcination procedure (Yu *et al.*, 2013). The photocatalytic results displayed that U100 exhibited the highest HCHO decomposition ratio (94%), as shown in (Fig. 2c). Through the calcination process, the interface amid TiO_2 and g-C_3N_4 was improved, allowing for better electrical conductivity. TiO_2 has a thin coating of g-C_3N_4 nanosheets (NSs), and the g-C_3N_4 NSs are in intimate contact with the TiO_2 substrate (Fig. 2e and f). The concentration of photoexcited ·OH was examined through the PL process in the presence of a probe molecule (terephthalic acid). With formaldehyde degradation activity under UV light and improved charge separation efficacy, the g-C_3N_4/TiO_2 nanocomposite surpasses pure TiO_2 and g-C_3N_4 photocatalysts. The VB_{h+} of g-C_3N_4 holes cannot generate ·OH because their VB potential is less positive than H_2O/·OH and ·OH radicals were formed from holes in VB of TiO_2 (Fig. 2d). However, the generation of ·OH intermediates in g-C_3N_4/TiO_2 hybrids cannot be

described by charge transfer via type II heterojunctions. The findings reveal a simple charge transfer via Z-scheme. Zheng *et al.* successfully fabricated CdS/Au/g-C_3N_4 Z-scheme ternary heterojunction using HCNS (Zheng *et al.*, 2015). A prominent emission peak was showed by PL characterization of the HCNS (Fig. 2g). Combining HCNS with CdS and Au resulted in a photocatalyst with much-reduced charge recombination, as seen by the rapid quenching of the intense PL. These results obtained from the highly efficient charge separation were afforded by the indirect Z-scheme heterojunction which was validated through photocurrent response (Fig. 2h). Au nanoparticles worked as an electron mediator, accelerating the transport of photoexcited e^--h^+ pairs from CdS to HCNS. Fabricated CdS/Au/g-C_3N_4 heterojunction has the maximum photocatalytic activity than CdS and HCNS nanoparticles. In order to shuttle the photoexcited e^-s between two SCs in Z-scheme, it is necessary to introduce electron mediators, as indicated above. It's important to note that the interface, in close contact, can serve as a mediator, much like electrons. The illustration of the proposed photocatalytic mechanism presented in (Fig. 2i).

Z-scheme heterojunctions have excellent, efficient charge separation efficiency and great redox ability, but they also have several limitations: conventional heterojunctions, Z-scheme Heterojunctions, and all-solid-state exhibit glaring flaws (Zhu *et al.*, 2017). Unlike the latter, the former is restricted towards the solution phase and is likely to choose alternative, less desirable charge-transfer paths. Under these conditions, the adequate photogenerated holes and electrons will be consumed by the redox pairs. In contrast, the photoinduced holes and electrons with lower abilities will be preserved, rendering the advantage of the classic Z-scheme over the type-II heterojunction (Paul *et al.*, 2019). Also, the redox pairs are unstable and prone to destructive reactions that might compromise the whole system. The redox couples are also sensitive to changes in pH and light, limiting their usefulness. The purpose of the ASS Z-scheme is to replace redox couples with nanoscale conductors, thereby removing the need for them and expanding the scheme's potential applications. Nonetheless, it has the same flaw (Wu *et al.*, 2017). While the all-solid-state Z-scheme may seem promising at first glance, its charge-transfer method differs from what is advertised (Ge *et al.*, 2019). When the potential difference between two photocatalysts is more significant, the driving force is greater, and e^- in the photo-catalyst with the higher CB potential will prefer to pass via the conductor to the photo-catalyst with the lower VB potential. If the conductor is not perfectly positioned between the two photocatalysts, electron transfer may still occur through the conductor to the surface. The Z-scheme family, of which ASS Z-scheme is a part, includes the vulnerable direct Z-scheme heterojunction (Kumar *et al.*, 2021).

2.1.3. S-scheme Heterojunctions

The latter group is rather extensive and includes the more common Z-scheme photocatalysts and the more exotic direct and ASS Z-scheme photocatalysts. Some ideas are borrowed from other fields during the first two generations. When a family's ancestors, such as conventional Z-scheme photocatalysts, have serious flaws, the offspring are sometimes wrongly assumed to have the same issues. Direct Z-scheme feels the shortcomings of conventional traditional and ASS Z-scheme photocatalystsalso felt by direct Z-scheme (Bao *et al.*, 2021; Zhang *et al.*, 2022). Here, a novel notion is preferred over Z-scheme and type-II heterojunction because it more accurately represents the photocatalytic mechanism. S-scheme heterojunctions, like type-II heterojunctions, are made up of two semiconductors with distinct band structures (SC-II and SC-I). However, this configuration transfers the charge through a different path (Shawky *et al.*, 2022; Wang *et al.*, 2022). In S-scheme heterojunction, hen two SCs were coupled together, the most efficient photoexcited e^--h^+ were stored in VB of SC-II and CB of SC-I, while the less useful photocarriers were recombined, resulting in a powerful redox reaction (Fig. 1f) (Kumar *et al.*, 2021; Zhang *et al.*, 2022). It is possible to describe the pathway by which charges move through an S-scheme as follows: (1) Compared to SC-I, SC-II has a more significant CB and VB position and a lower work function. Electrons from the SC-II spontaneously diffuse into the SC-I, forming an accumulation and depletion layer close to the interface in the two SCs. SC-I have a negative charge, while SC-II has a positive one. Simultaneously, an axial electric field is generated, with the direction of the area being from SC-I to SC-II. This internal electric field (IEF) has the opposite effect of what would happen with external electric fields, speeding up the transference of photoinduced e^- from SC-I to SC-II. (2) It is optimal for SC-I and

SC-II to have identical Fermi energies when they interact. As a result, the Fermi levels of SC-I and SC-II go upward and downward, correspondingly (Xu *et al.,* 2020). Photoexcited h^+ in VB of SC-II and e^- in CB of SC-I at the edge region were forced to recombine due to the band bending, which can be understood by imagining water flowing downhill. (3) Owing to the Coulombic interaction amongst photocarriers, the photogenerated CB e^- of SC-I and VB h^+ of SC-II are likely to recombine at the border (Bao *et al.,* 2021; Wang *et al.,* 2021; Xu *et al.,* 2020). In conclusion, the recombination of e^- in the CB of SC-I and h^+ in the VB of SC-II is driven by the Coulombic attraction, band bending, and IEF. As a result, the photogenerated e^- and h^+ in the SC-II CB and the SC-I VB, respectively, are maintained for photocatalytic processes while the surplus electrons and holes are removed by recombination. The introduction of a new mechanism, specifically, the S-scheme heterojunction has also been explored on the topic at hand. According to their band structure, photocatalysts are classified as either OP or RP in this system. We find that not all photoinduced holes and electrons are useful as we investigate this phenomenon. This system keeps the valuable elements and gets rid of the useless ones. Here, we have an instance where charge segregation and strong redox capability go hand in hand (He *et al.,* 2020). Long-term light adsorption, effective charge separation, and high redox potentials may be attained. To explain this occurrence, the authors not only present the concept of the S-scheme but also give experimental data in support of it. When compared to type-II heterojunctions and members of the Z-scheme family, the charge-transferal mechanism in S-scheme is significantly distinct, leading to improved photocatalytic performance (Kumar *et al.,* 2021). In our opinion, this proposal is the better option among all other heterojunction systems.

Deng and his peer group fabricated 2D/2D g-C_3N_4/$ZnIn_2S_4$ (CN/ZIS) S-scheme heterojunction with boosted interfacial charge migration and separation by facile hydrothermal process and employed for the removal of TC (Deng *et al.,* 2022). The formed S-scheme heterojunction photocatalysts was an efficient way to boost the photodegradation ability of photocatalyst via efficient and enhanced photo-redox capacity and higher charge transmission efficacy. The morphological and microstructures results showed excellent interaction among ZIS (average size of ~20 nm) and CN via deposition of small-sized ZIS NSs with low agglomeration on the shell of ultrathin g-C_3N_4, which ultimately enhanced contact area among both NSs. Through BET analysis, 81.56 $m^2\ g^{-1}$ and 43.80 $m^2\ g^{-1}$ SSA (specific surface area) were observed for pristine ZIS and CN, respectively and after the formation of nanocomposite SSA of CN/ZIS-X photocatalyst progressively enhanced SSA with the increase of ZIS content (Fig. 3a). The enhanced SSA, average pore diameter and total pore volume of CN/ZIS-10 recommended more photocatalytic locates to simplify the interfacial reaction. The photodegradation results also confirmed that within 120 min of visible light illumination, the observed degradation efficiencies were 62.42%, 67.73%, 79.91%, 89.59%, 93.41%, and 88.53% for CN, ZIS, CN/ZIS-30, CN/ZIS-5, CN/ZIS-10, and CN/ZIS-15 correspondingly as displayed in Fig. 3b. Amongst all fabricated photocatalysts, the CN/ZIS-10 nanocomposite exhibited higher removal efficacy due to the higher photocarriers separation and fast interface charge relocation via the formation of S-scheme charge transfer route. Validation of efficient charge separation and migration in synthesized photocatalysts was done through PL (Fig. 3c), photocurrent and electrochemical impedance spectroscopy (EIS) analysis. CN/ZIS-10 nanocomposite has higher PL intensity and photocurrent density, while the lowest Nyquist plot arc was achieved for CN/ZIS-10. The proposed S-scheme photocatalytic mechanism for CN/ZIS-10 demonstrated in Fig. 3d and e presented that $^{\bullet}O_2^-$ and $^{\bullet}OH$ radicals were the only reactive species participating in the photodegradation process (confirmed *via* scavenging experiments). Another report on the photodegradation of levofloxacin (LVF) was provided by Yang *et al.* via preparation of yolk-shell spheres $CuCo_2S_4$ entrenched with S-scheme heterostructure of V_2O_5-accumulated on crumpled g-C_3N_4 (VO-WCN) (Yang *et al.,* 2022). The work reported tremendous photodegradation capability because of extensive light absorption, excellent reduction capability and (photo)electrochemical benefits of $CuCo_2S_4$ (CCS) of thio-spinels. The work presented embedding of the synthesized CCS on S-scheme VO-WCN heterostructure by using a repetitive two-step method (solvothermal followed by neutral calcination) to form VO-WCN@CCS nanocomposite. The synthesized photocatalysts had superb SSA calculated through the BET isotherm method (S_{BET}), i.e. 11.3, 120.2, 43.0, 96.3, 115.1, and 93.7 m^2/g for VO, WCN, CCS, WCN@CCS(30), VO-WCN, and VO-WCN@CCS(30), respectively (Fig. 3h). Amongst all prepared

photocatalysts, the optimized VO-WCN@CCS(30) nanocomposite (30 wt% CCS loading) presented 98% LVF removal, which was 9.9, 7.2, and 19.1 folds higher than bare WCN, VO, and CCS, correspondingly within 120 min. Incremented LVF degradation efficacy of nanocomposite was attributed to effective charge migration and departure due to its IEF at the WCN, VO, and CCS interface in S-scheme heterostructure, which diminished the charge recombination rate as shown in the charge-flow transfer diagram in Fig 3i. Similarly, the outstanding stability of heterogeneous VO-WCN and its e^- donor ability seized self-oxidation of CCS. PL and electrochemical quantification (TPC and EIS) analysis validated the low recombination rate and enhanced charge separation and transferal ability in the VO-WCN@CCS nanocomposite (Fig. 3f and g).

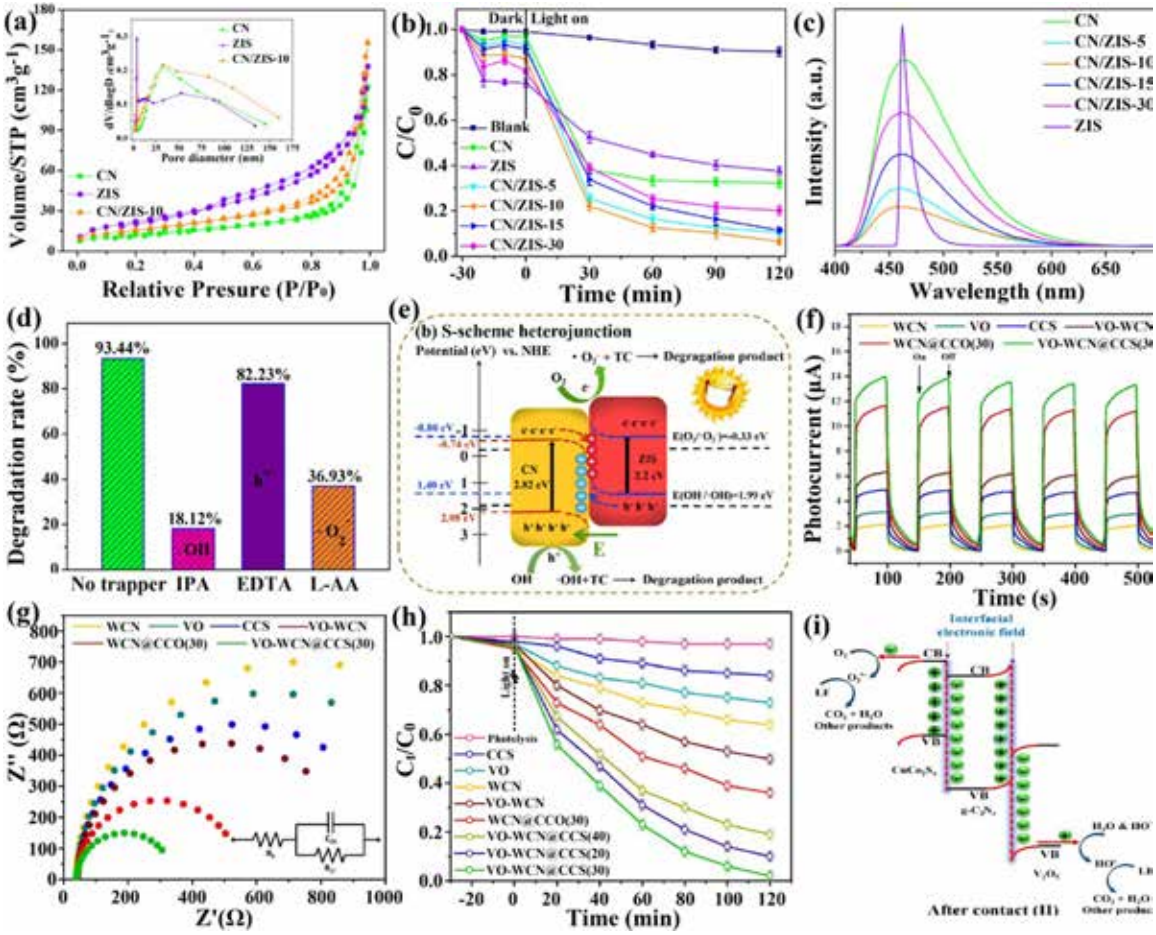

Figure 3. (a) BET isotherms results with inset showing pore diameter distribution curves of CN, ZIS and CN/ZIS-10 photocatalysts, (b) TC degradation results and (c) PL spectra of all prepared photocatalysts, (d) Scavenging results showing TC degradation and (e) Graphical representation of visible light assisted possible charge transfer mechanism of TC degradation using CN/ZIS-10 photocatalyst, Reprinted with permission from Elsevier (License No. 5431271201890) (Deng *et al.,* 2022). (f) Photocurrent and (g) EIS spectra and (h) Photodegradation results of all prepared photocatalysts, (i) Illustration of charge-transfer mechanism in VO-WCN@CCS nanocomposite via built-in IEF, Reprinted with permission from Elsevier (License No. 5431280254096) (Yang, X. *et al.,* 2022).

Lu and Wang designed core-shell microsphere $CuWO_4$@g-C_3N_4 with S-scheme for the photoreduction of CO_2 (Lu *et al.*, 2023). The work presented the preparation of core-shell microspheres $CuWO_4$@g-C_3N_4 through annealing and hydrothermal method (Fig. 4a). $CuWO_4$@g-C_3N_4 nanocomposite attained much superior photocatalytic performance to the single photocatalysts. The

enhanced CO_2 photoreduction was due to increased SSA, enhanced visible light absorption, and enriched CO_2 adsorption proficiency. The observed BET SSA of $CuWO_4$, g-C_3N_4, and $CuWO_4$@g-C_3N_4 was 21, 34, and 50 m^2g^{-1} with a pore volume of 0.11, 0.08 0.20 cm^3g^{-1}, respectively. During CO_2 photoreduction, the highest achieved CO yield rate for $CuWO_4$@g-C_3N_4 nanocomposite was 2.7 folds than pristine g-C_3N_4, i.e. 4.15 µmol $g^{-1}h^{-1}$ and 1.56 µmol $g^{-1}h^{-1}$ for $CuWO_4$@g-C_3N_4 and g-C_3N_4 photocatalysts, respectively (Fig. 4d). Using theoretical studies, it was indicated that reduction and hydrogenation of *OCHO to *HCOOH were taken in higher E_b of 0.39 eV which was more significant than CO (0.24 eV) and also contributed in high selectivity for CO yield. Furthermore, in $CuWO_4$@g-C_3N_4 S-scheme heterojunction, facilitated photoinduced charge carrier's separation (EIS and validated through photocurrent) and recognized strong redox ability contributed to superior CO_2 photoreduction ability (Fig. 4b and c). The EPR analysis verified the S-scheme heterojunction by DMPO-˙OH and DMPO-$˙O_2^-$ EPR spectra (Fig. 4e and f), revealing strong DMPO-˙OH and DMPO-$˙O_2^-$ signals in $CuWO_4$ and g-C_3N_4, respectively. This confirmed that $CuWO_4$ was an oxidative semiconductor, while g-C_3N_4 was a reductive semiconductor. The proposed mechanism is presented in (Fig. 4g). To reconnoitre H_2 production, and a S-scheme g-C_3N_4/$CoTiO_3$ heterojunction was employed by Meng and his research group (Meng *et al.*, 2022). In this work, S-scheme g-C_3N_4/$CoTiO_3$ nanocomposite was used during photocatalytic H_2 production, and no sacrificial agents were utilized. 118 µmol $g^{-1}h^{-1}$ H_2 production rate was obtained with 1.5 wt% optimum loading of $CoTiO_3$ in g-C_3N_4/$CoTiO_3$ (CCT-1.5) (Fig. 4h). The increased H_2 production rate mainly credited to the prolonged light garnering due to amalgamated visible light driven property of $CoTiO_3$ and efficient charge departure plus relocation with strong redox capability, prompted by the S-scheme charge transfer way (confirmed through PL and photocurrent) (Fig. 4i and j). As presented in Fig. 4k, $CoTiO_3$ have lower Fermi potential than CN but when both SCs $CoTiO_3$ and CN came in contact with each other, transference of e^- took place from CN to $CoTiO_3$ owing to the difference in their Fermi levels. After some time, when Fermi levels align, the charge migration attained equilibrium at the end. In this situation, the –ve charged ions accumulated on the $CoTiO_3$ side of the edge, whereas +ve charged ions were collected on the other side of CN. So, an IEF is and produced from CN to $CoTiO_3$ transversely through the interface. Consequently, band bending in CB and VB of both semiconductors took place at the interface region and led to the construction of an S-scheme heterostructure, as illustrated in Fig. 4k.

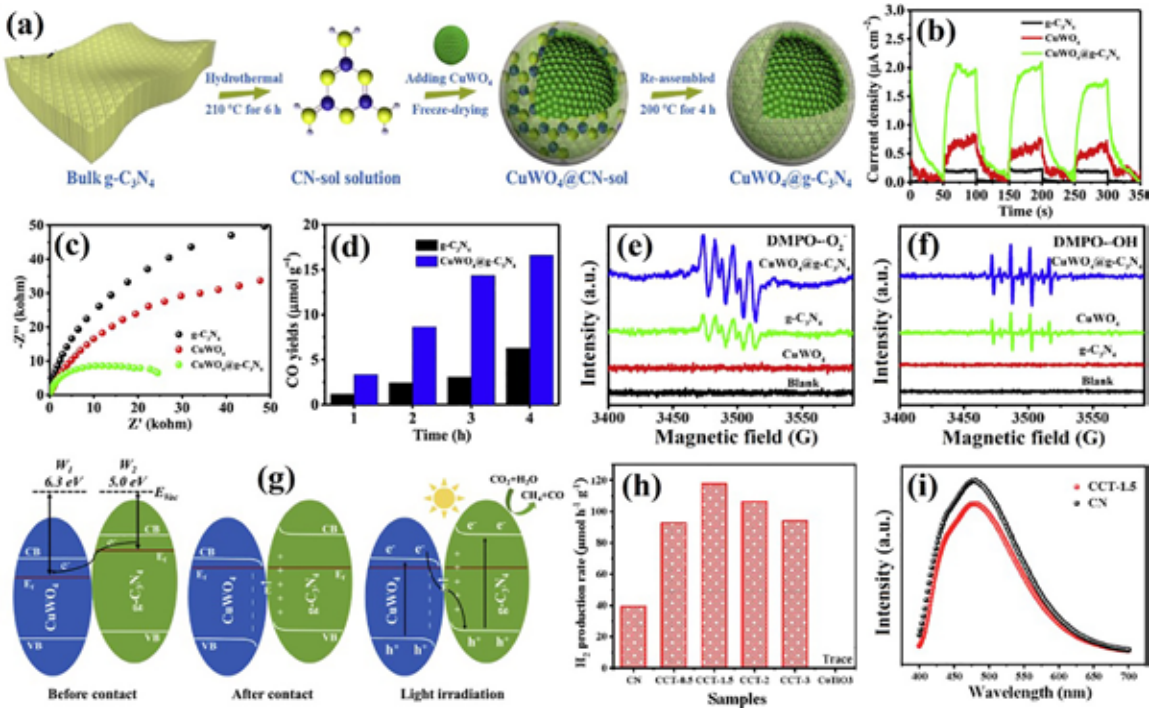

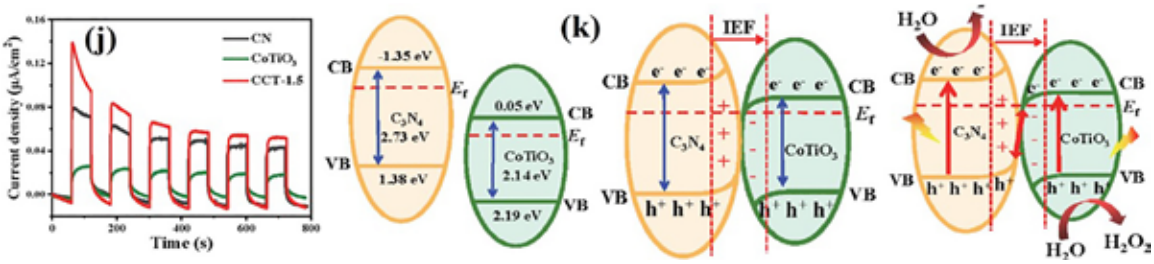

Figure 4. (a) Diagram showing preparation route of $CuWO_4$@g-C_3N_4 core-shell nanocomposite, (b) photocurrent and (c) EIS spectra of samples, (d) Bar graph presenting photoreduction of CO_2 into CO, (e) DMPO-O_2^- and (f) DMPO-OH EPR spectra, (g) The band arrangement among $CuWO_4$ and g-C_3N_4 photocatalysts (before, after contact, and in the presence of light illumination) with proposed mechanism displaying photocarriers migration among $CuWO_4$ and g-C_3N_4 in $CuWO_4$@g-C_3N_4 heterojunction, Reprinted with permission from Elsevier (License No. 5431280870375) (Lu *et al.,* 2023). (h) Results showing photocatalytic H_2 production by CN, $CoTiO_3$, and CCT-*x* (*x* = 0.5, 1.5, 2, 3) photocatalysts, (i) PL spectra and (j) Photocurrent spectra of prepared photocatalysts, (k) Graphic representation of the band alignments in CN and $CoTiO_3$ before, after contact, and under light irradiation presenting photocatalytic S-scheme charge transfer route in CCT-1.5 nanocomposite via the formation of IEF, Reprinted with permission from Elsevier (License No. 5431281145797) (Meng *et al.,* 2022).

3. APPLICATIONS OF S-SCHEME BASED g-C_3N_4 HETEROJUNCTION PHOTOCATALYSTS IN POLLUTANT DEGRADATION AND ENERGY CONVERSION

The significant fundamental problems in type-II heterojunction ad the Z-scheme family have upsurged the emergence of S-scheme-based photocatalytic applications. This section discusses the worldwide issues of energy conservation and waste-water treatment with progressive research on g-C_3N_4 C_3N_4-based S-scheme heterostructures. The photocatalytic efficiency mainly depends on the utilization of light photons to improve oxidation/reduction reaction rates for sufficient generation of reactive oxidative species (Shawky *et al.*, 2022). The development of a desirable S-scheme heterojunction is well-explored using g-C_3N_4 photocatalyst owing to its inherent tunable electronic structure and visible light active band gap with prospected redox potentials (Xu *et al.*, 2020).

3.1. Pollutant degradation

The presence of different kinds of hazardous pollutants in wastewater is one of the significant problems in recent times. The speedy growth of industries and population has severely affected drinking water resources (Afroz *et al.*, 2014; Li *et al.*, 2019). Numerous pollutants, such as dyes, antibiotics, phenols, heavy metals, etc., are continuously being released, which are entering into the drinking water resources and polluting them. These pollutants have several hazardous effects on the life of all living organisms as well as on the environment, e.g. the indestructible waste of the pharmaceutical industries and the excreted drug deposits by societies due to meagre metabolic action caused the release of these contaminants into environmental sources and also caused the growth of antibiotic-resistant pathogens (Andersson, 2003; Chen *et al.*, 2018; Khachatourians, 1998). Hence, photo-oxidation is recognized as an effective way to solve this major issue and abatement of environmental contaminants. Notably, the photo-oxidation accelerated under visible light is more promising as visible light is easily accessible and harmless to humans (Wang *et al.*, 2020; Yang *et al.*, 2021). Previously, we have discussed the advantages of S-scheme heterostructure and g-C_3N_4-based nanocomposites in the field of photocatalysis. So, in this section, we are the uses of S-scheme based g-C_3N_4 heterojunctions for eradicating various noxious waste existing in wastewater, e.g. antibiotics, dyes, phenols and heavy metals etc.

3.1.1. Antibiotics removal

Nowadays, the inappropriate and excessive use of several antibiotics has threatened the life of living beings *via* polluting water resources. These are considered major components of water pollution and environmental concerns. By 2020, the utilization

of pharmaceuticals has reached up to 4500 billion tons world widely, and a minimum of 3000 pharmaceutical species have been found in water and wastewater (Chavoshani *et al.,* 2020). The high pharmaceutical consumption and persistent and unsafe disposal the water resources have harmful and dreadful consequences on the environment and living organisms (Qiao *et al.,* 2018). As an emerging pollutant, antibiotics have gradually turned out to be the centre of attention. Several kinds of antibiotics are polluting water resources such as tetracycline, norfloxacin (NOR), diclofenac (DCF), Levofloxacin (LF), (Iwuozor *et al.,* 2021; Vieno *et al.,* 2014; Xia *et al.,* 2022; Zhang *et al.,* 2019), etc. Hence, removal of these; in this context, g-C_3N_4 based photocatalytic materials has been considered asantibiotic contaminants highly required; in this context, g-C_3N_4 based photocatalytic materials has been considered an efficient and potential candidate. For the removal of theses pharmaceutical pollutants, several reports on S-scheme based g-C_3N_4 heterojunctions were published (Li *et al.,* 2022). The reported data found that preparation and utilization of S-scheme-based g-C_3N_4 heterojunctions is a way to mineralize these harmful pollutants into non-toxic products. TC is extensively utilized and produced antibiotic for living organisms (Vinesh *et al.,* 2020; Xu *et al.,* 2021). However, TC is more advantageous to human and animal health. Still, untreated and over usage of TC affect the ecological balance as it is not liable to biodegradation and causes the production of drug-resistant bacteria (Ahmad *et al.,* 2021; Davies *et al.,* 2021). The eradication of TC pollutant from water resources is highly required, and the researchers did several works on photocatalytic TC removal. For example, Preeyanghaa and his research group reported the degradation of TC using an S-scheme 1D/2D rod-like g-C_3N_4/V_2O_5 (RCN-VO) heterojunction (Preeyanghaa *et al.,* 2022). Ultrasound-assisted thermal polycondensation technique was used to prepare S-scheme RCN-VO nanocomposite. The photodegradation results presented in Fig. 5a displayed complete removal of TC, i.e. 100% within 60 min of visible light exposure and ultrasound from wastewater using RCN-VO-2 nanocomposite. The results also confirmed ~1.5 times higher TC removal efficacy via sonophotocatalytic process than sonocatalytic and photocatalytic processes utilizing RCN-VO nanocomposite. The augmented sonophotocatalytic degradation efficacy of RCN-VO was ascribed to 1D/2D nanostructure, and the formed S-scheme charge transfer route among RCN and VO, in which the transference of excited e^- took place from RCN to VO through the RCN-VO border. However, the accumulated e^- in RCN and h^+ in VO strongly participated in the redox processes generating free radicals to eradicate TC molecules. It was also observed that creating S-scheme heterojunction via a built-in electric field, band bending and Coulombic interaction concurrently enabled charge separation with a reduced recombination rate. The highest charge separation and low recombination rate was observed for RCN-VO2 nanocomposite, validated through PL and EIS analysis as shown in Fig 5b and c. The observed TC sonophotocatalytic removal efficacy of RCN-VO3, RCN-VO2, RCN-VO1, RCN, and CN was 85%, 98%, 70%, 34%, and, 20%, respectively. The presented photocatalytic mechanism in as shown in Fig. 5d revealed the major role of h^+, $^{\bullet}O_2^-$ and $^{\bullet}OH$ radicals during sonophotocatalytic degradation process of TC using RCN-VO2 nanocomposite. Another antibiotics, Norfloxacin (NOR) and Levofloxacin (LF), family members of fluoroquinolones (FQs) antibiotics, are widely consumed for a several infectious diseases owing to its minimal complication and wide-spectrum antibiotic characteristics (Wammer *et al.,* 2013). It was found in many water resources (Chen *et al.,* 2021; Du *et al.,* 2017), and its long-term survival in the environs persuades the production of antibiotic-resistant pathogens (Chen *et al.,* 2018; González-Pleiter *et al.,* 2013). For the photocatalytic removal of norfloxacin (NOR) pollutant, a 2D/2D N-ZnO/g-C_3N_4 (2D/2D N-ZnO/CN) S-scheme heterostructure was fabricated by calcination of ZIF-L/CN composites (Zhang *et al.,* 2022). The results stated that the bare CN and N-ZnO exhibited low charge separation efficacy but after the S-scheme heterojunction formation with N-doped ZnO, the photocarriers separation and transference rate increased at the border due to the generation of IEF, directed from CN to N-ZnO. The observed degaradtion efficacy of S-scheme heterostructure i.e. 15% NZCN/vis system was 96.4% within 90 min, however for CN and N-ZnO the degradation rate was 55.4% and 57.7%, respectively Fig. 5e. Besides, NOR degradation, the researcher also examined the photocatalytic efficacy of 15% NZCN/vis system towards enrofloxacin (ENR), levofloxacin (LVF), and ciprofloxacin (CIF) and the attained photodegradation rate was more than 90% in 90 min (Fig. 5f). NOR degaradtion results displayed 4.15 and 4.65 folds higher rate constant of 15% NZCN compared to CN and

N-ZnO, individually. During NOR photodegradation process, the reactive species participated were h^+ and $^{\bullet}O_2^-$ radicals validate through quenching and electron proton resonance (EPR) results. The NOR degradation mechanism showing the S-scheme charge transfer route among CN and N-ZnO photocatalysts were represented in Fig. 5g Through mechanism it can be explained that the S-scheme heterostructure reserved the redox potential of photocarriers for further reaction and resulted in higher charge separation and transmission. In the similar way there are reports on cefixime (CFX) antibiotic photocatalytic degradation using green and environmentally friendly S-scheme heterostructure of Bi_2WO_6/g-C_3N_4 (BC) and Bi_2WO_6/TiO_2 nanocomposite (Gordanshekan *et al.*, 2023). In this work, Gordanshekan and his peer has compared the photodegradation ability of two different nanocomposite (Bi_2WO_6/g-C_3N_4 and Bi_2WO_6/TiO_2) synthesized via hydrothermal treatment. The degradation results revealed 94 % and 91 % CFX removal efficacy of BC 60% and BT 12.5% within 135 min of photocatalytic reactions. The PL, photocurrent response, EIS, and LSV results presented low recombination rate and enhanced photocarriers separation and transference ability in BC 60% compared to BT 12.5%. Due to S-scheme heterostructure formation the nanocomposite exhibited higher charge separation and transferal ability due to formation of IEF among binary photocatalysts as presented in Fig. 5h and i. The scavenging tests confirmed the noteworthy role of $^{\bullet}OH$ and $^{\bullet}O_2^-$ radicals in Bi_2WO_6/g-C_3N_4 but for Bi_2WO_6/TiO_2, $^{\bullet}OH$ and e^- were the major reactive species during photodegradation process.

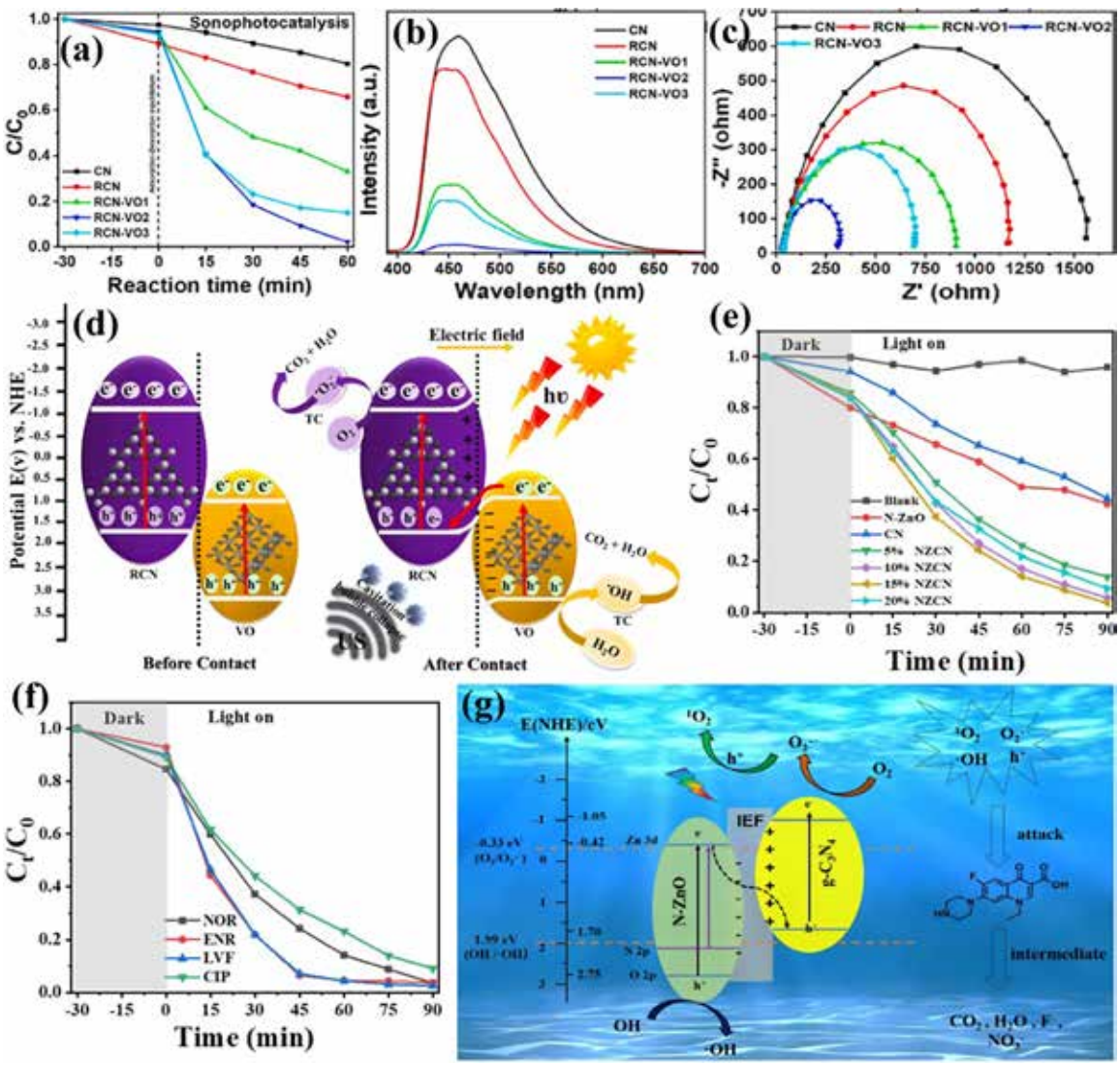

 https://doi.org/10.37819/nanofab.008.292

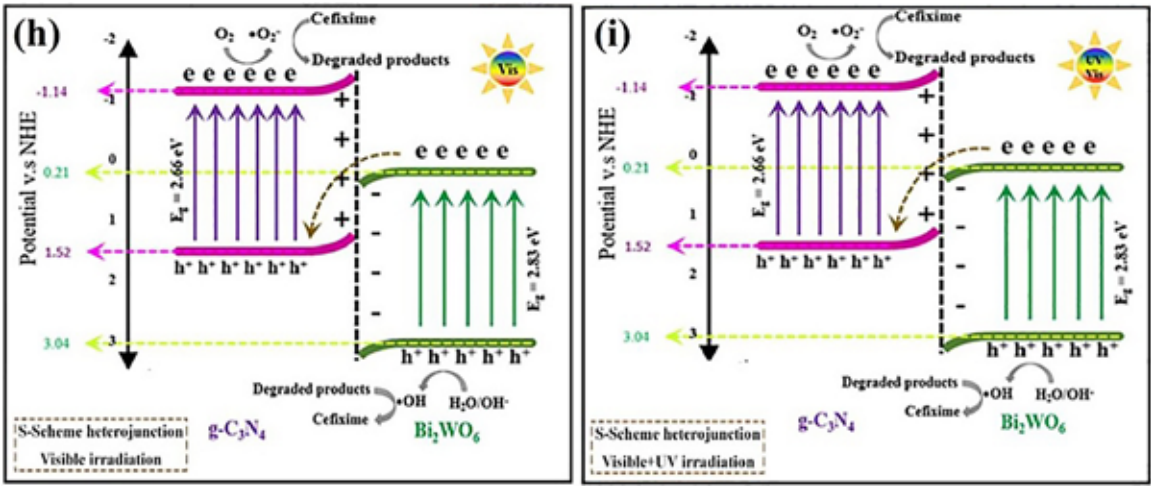

Figure 5. (a) C/C0 plots presenting sonophotocatalytic TC degradation results using the synthesized photocatalysts, (b) PL and (c) EIS spectra of CN, VO, RCN, and RCN-Vo_x photocatalysts, (d) Schematic diagram of S-scheme based sonophotocatalytic degradation mechanism of TC using 1D/2D RCN-VO photocatalyst, Reprinted with permission from Elsevier (License No. 5431281439729) (Preeyanghaa *et al.,* 2022). (e) Photodegradation results of NOR antibiotic using fabricated photocatalysts, (f) Photodegradation results of NOR, ENR, LVF, and CIP, and (g) The proposed photodegradation mechanism of NOR using S-scheme based 15% NZCN/vis photocatalytic system, Reprinted with permission from Elsevier (License No. 5431290386686) (Zhang *et al.,* 2022). The proposed S-scheme charge transfer route in BC 60 % nanocomposite (h) under visible irradiation and (i) UV–vis irradiation, Reprinted with permission from Elsevier (License No. 5431290789718) (Gordanshekan *et al.,* 2023).

3.1.2. Textiles dyes removal

The existence of different textile dyes in water resources caused harmful effects on living organism life. The dyes are extensively used by small-scale to large-scale industries, with the production of 1,000,000 tons world widely (Maheshwari *et al.,* 2021; Tkaczyk *et al.,* 2020). Regardless of the significance of industries to humanss, these are the major global polluters that consume fuels and chemicalsto high extents (Kumar, 2022; Mani *et al.,* 2019). Several reports on photocatalytic dye degradation have been reported using g-C_3N_4-based S-scheme photocatalysts. Li *et al.* performed the methyl orange (MO) degradation using a hierarchical flower-like 0D/3D g-C_3N_4/TiO_2 (TiO_2/CNQDs) S-scheme heterojunction which was low-cost and eco-friendly (Li, Yuan *et al.,* 2022). This work combined a non-toxic, metal-free 0D carbon nitride quantum dots (CNQDs) and 3D flower-like TiO_2 microspheres to form a heterostructure with improved visible-light harvesting ability, resilient redox ability, larger SSA and pore volume. The broad energy gap of TiO_2 and higher recombination rate of photocarriers limits its photoactivity under solar light, but after combining with g-C_3N_4 the photodegradation ability against MO dye increased. This was attributed to the prepared S-scheme heterostructure which has shown boosted charge separation, and transference of photocarriers with reticent charge recombination rate verified through photocurrent and EIS analysis (Fig. 6a and b). Among all the prepared photocatalysts, TiO_2/CNQDs-3 nanocomposite has shown superior photodegradation ability and excellent light absorption intensity with transient photocurrent density and charge separation. The degradation results presented the highest MO degradation rate constant value for the TiO_2/CNQDs-3, i.e. first-order reaction kinetics that was 5.4 and 2.2 folds higher pure TiO_2 and P25, correspondingly (Fig. 6c). The photodegradation mechanism indicated the existence and essential part of h^+, $^{\bullet}OH$, and $^{\bullet}O_2^-$ radicals in formed S-scheme heterojunction (Fig. 6d). Similarly, methylene blue (MB) dye degradation was reported by Van and his research team by employing a novel S-scheme CdS/g-C_3N_4 nanocomposite possessing enriched visible-light photodegradation ability (Van *et al.,* 2022). The CdS/g-C_3N_4 nanocomposite was constructed using

a facile solvothermal route to minimize the limitations of both bare photocatalysts, i.e. inherent high recombination rate of photocarriers and photocorrosion of CdS. The degradation results showed that MB photodegradation efficiency was much higher for CdS/g-C_3N_4 (96.89%) however, CS and CN had 45.58% and 12.85% removal efficacy within 120 min of 30W LED light lamp, as shown in Fig. 6e. Besides this the research group also observed 98.66% and 99.85% MB removal efficacy after 180 and 60 min of 40W LED lamp and natural sunlight illumination (Fig. 6f). The enhanced removal efficacy of nanocomposite owed to the efficient photocarriers transportation through the S-scheme pathway which has extended the lifespan of photocarriers, delocalized oxidative h^+ on CdS_{CB} to prevent photocorrosion and preserved the higher reactive oxygen species for different photocatalytic reactions as displayed in Fig. 6g. Through quenching experiments, the substantial part of $^{\bullet}OH$, and $^{\bullet}O_2^-$ radicals were confirmed which was also illustrated in the proposed photocatalytic mechanism.

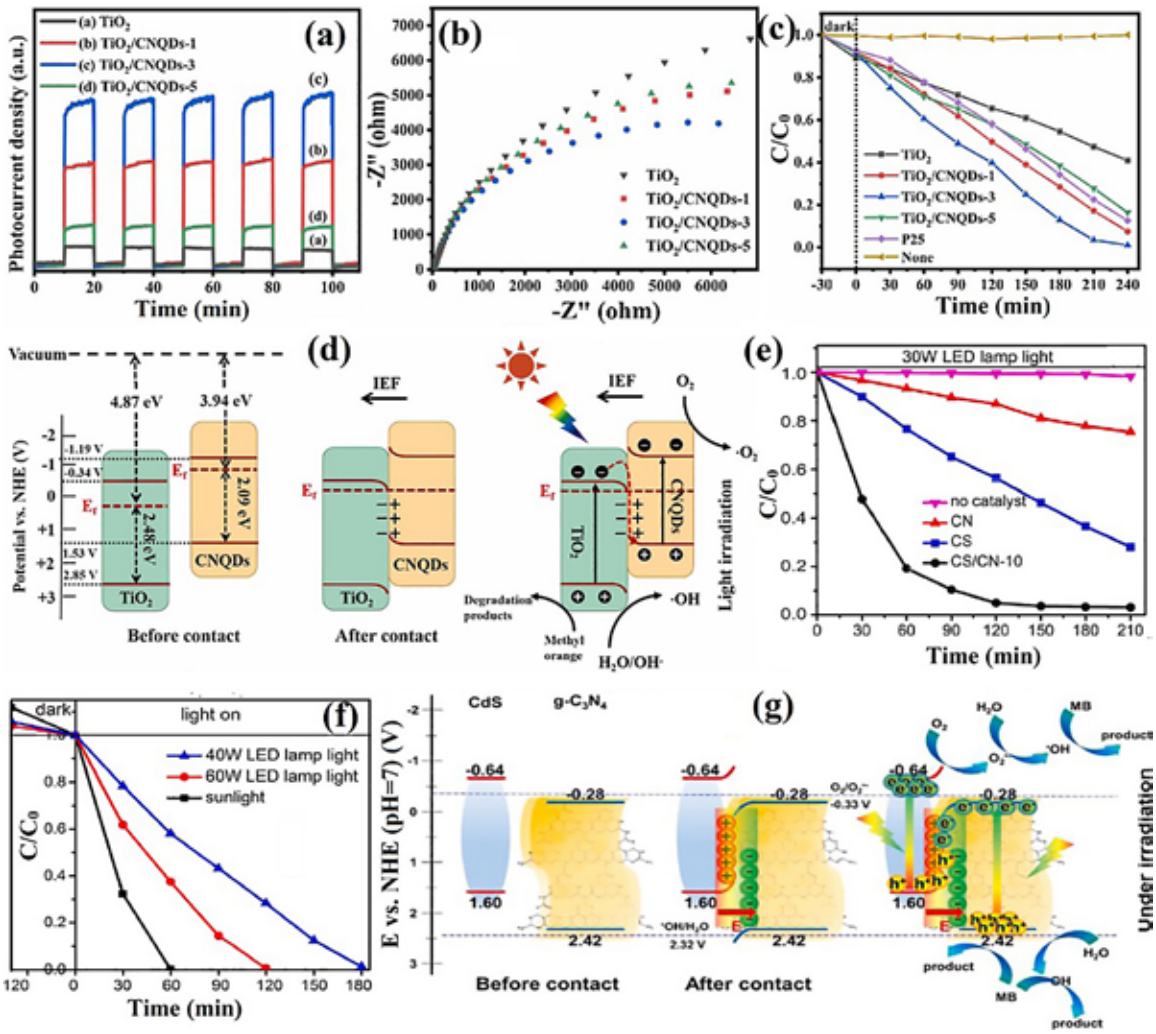

Figure 6. (a) The photocurrent and (b) EIS spectra of TiO_2 and the TiO_2/CNQDs photocatalysts, (c) The MO photodegradation results of TiO_2/CNQDs-x, pure TiO_2 and P25, (d) The proposed MO photodegradation mechanism of TiO_2/CNQDs-3 nanocomposite (before, after and under light illumination), Reprinted with permission from Elsevier (License No. 5431301087156) (Li, Yuan *et al.,* 2022). (e) MB photodegradation results using prepared photocatalysts under 30W LED light exposure, (f) Influence of the different light sources on the MB degradation, (g) Possible charge transfer route in S-scheme g-C_3N_4/CdS nanocomposite (before, after and under light illumination), Reprinted with permission from Elsevier (License No. 5431301449278) (Van *et al.,* 2022).

 https://doi.org/10.37819/nanofab.008.292

Another report on a visible light-assisted S-scheme CdS-g-C_3N_4-graphene aerogel (CdS-g-C_3N_4-GA) heterostructure was given by Liu and his research team to eradicate RhB (Liu *et al.*, 2021). The researchers have also tested their prepared photocatalysts for H_2 production and found that CdS-g-C_3N_4-GA S-scheme heterostructure has shown the highest photocatalytic ability compared to bare photocatalysts. The enhanced degradation efficacy and H_2 evolution rate ere credited to S-scheme heterojunction resulting from the strong IEF, which enhanced the charge separation proficiency and light harnessing ability of photocatalysts. In ultrasonication-prepared S-scheme photocatalysts, the incorporated GA as electron acceptors assisted the efficient electron transference podium in boosting the photocarriers separation rate, proved through photoelectrochemical analysis (Fig. 7a). The observed H_2 hydrogen evolution rate from H_2O splitting was 24.79, 36.32, 69.77 and 86.38 μmol $h^{-1}g^{-1}$ for g-C_3N_4, CdS, CdS-GA and CdS-g-C_3N_4-GA, respectively under 4 h of visible light exposure, as shown in Fig. 7b. Similarly, RhB degradation results have presented 7.43%, 20.43% and 91.41% RhB degradation efficiency for g-C_3N_4, CdS and CdS-g-C_3N_4-GA photocatalysts within 50 min of light irradiation (Fig. 7c). CdS-g-C_3N_4-GA photocatalyst had superior degradation efficacy due to S-scheme charge transfer pathway and integration of g-C_3N_4, which promoted the visible light harnessing ability and charge carriers separation rate. Additionally, the possible photocatalytic mechanism shown in Fig. 7d and e presented the band banding and S-scheme charge transferal route among the CdS and g-C_3N_4 photocatalysts in the existence of electron mediator GA. Also, the perovskite-type $SrFeO_3$/g-C_3N_4 S-scheme nanocomposite (prepared by simple calcination method) was utilized to remove Acid Red B dye (Hu *et al.*, 2022). The work explored that excellent photocatalytic ability was attained when the mass ratio was 3:2 for g-C_3N_4 and $SrFeO_3$ with a calcination temperature of 500 ºC for 3 h. The attained Acid Red B dye degradation efficacy was 80.2% for prepared $SrFeO_3$/g-C_3N_4 under UV light illumination that was 3.68, 1.36 and 1.23 folds greater than bare $SrFeO_3$, g-C_3N_4 and uncalcined $SrFeO_3$/g-C_3N_4, correspondingly (Fig. 7f-h). Furthermore, using photocurrent (Fig. 7i) and PL experiments higher charge separation and relocation proficiency was observed for calcined $SrFeO_3$/g-C_3N_4 nanocomposite. The reactive species validation was done through the scavenging experiment, which specified a substantial role of $^{\bullet}O_2^-$ radicals during the photodegradation process in $SrFeO_3$/g-C_3N_4 S-scheme heterojunction (Fig. 7j). As presented in $SrFeO_3$/g-C_3N_4 S-scheme photocatalytic system, the enhanced photocarriers separation and immigration efficacy significantly reduced the undesirable recombination of photocarriers (Fig. 7k).

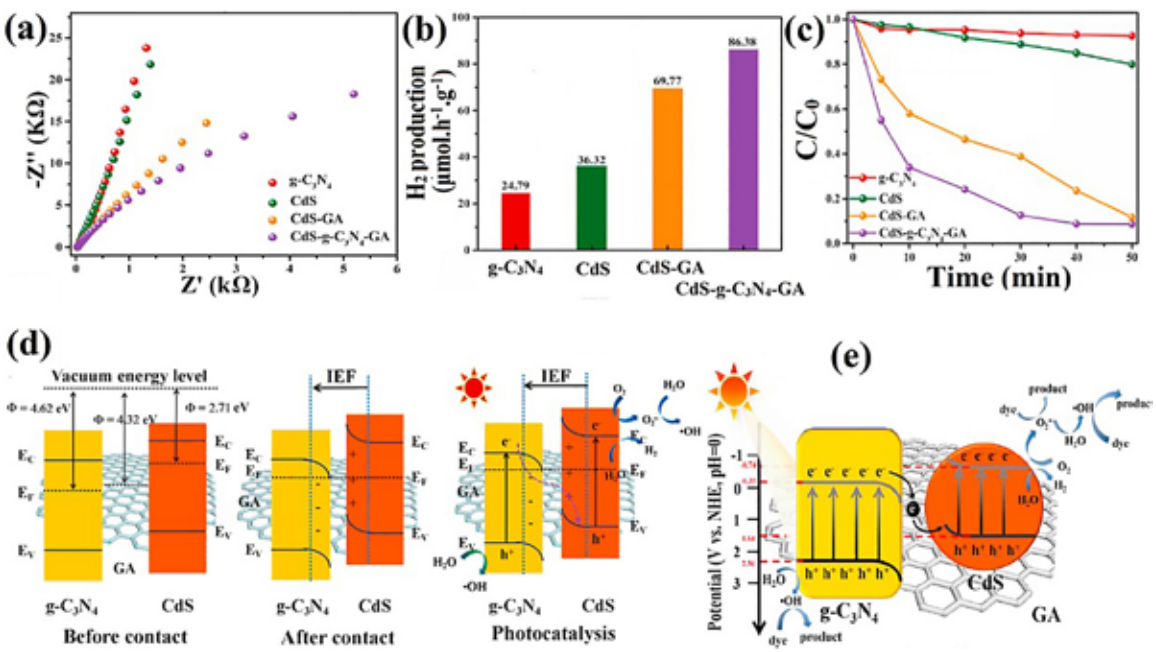

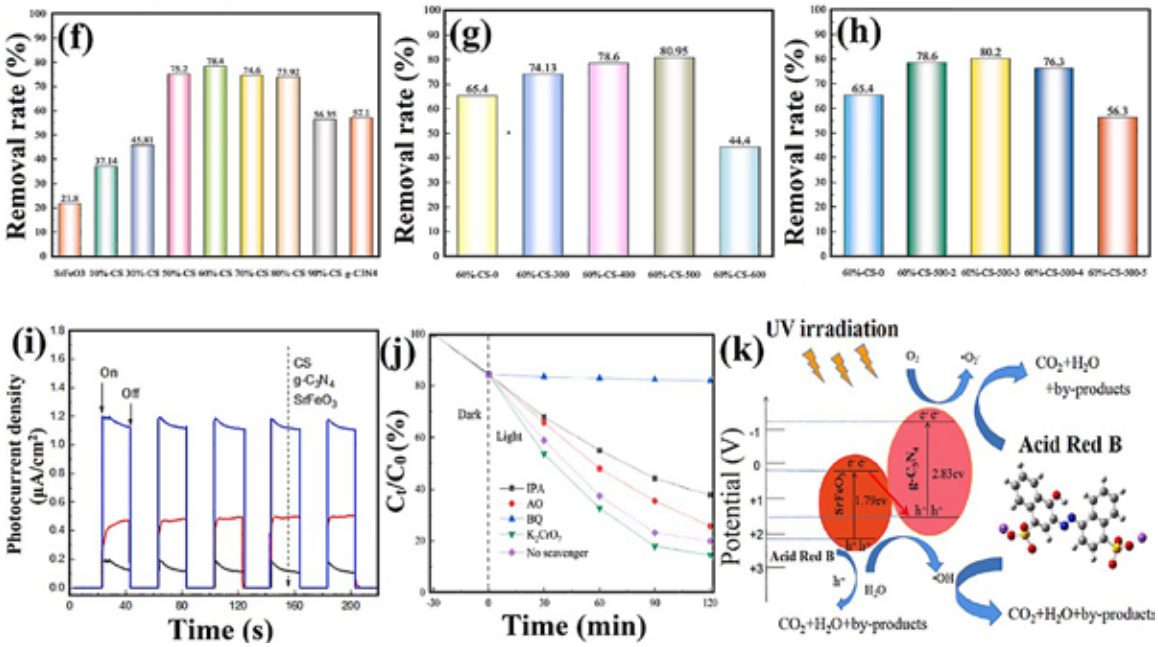

Figure 7. (a) EIS spectra of g-C_3N_4, CdS, CdS-GA, and CdS-g-C_3N_4-GA photocatalysts, (b) Results showing photocatalytic H_2 production from H_2O splitting and (c) RhB photodegradation using all prepared photocatalysts, (d) Graphic representation of work functions of CdS and g-C_3N_4 before contact, after contact (built-in IEF among GA, CdS and g-C_3N_4) and S-scheme charge migration route amongst CdS-g-C_3N_4-GA photocatalyst beneath visible light illumination, (e) Possible photodegradation mechanism of the fabricated CdS-g-C_3N_4-GA S-scheme heterojunction, Reprinted with permission from Elsevier (License No. 5433781454448) (Liu *et al.,* 2021). (f) Acid Red B photodegradation results using different composite, (g) at different calcination temperatures and (h) at other calcination times using $SrFeO_3$/g-C_3N_4 nanocomposite with varied ratios, (i) Photocurrent spectra of CS, g-C_3N_4 and $SrFeO_3$, (j) Scavenging results presenting the role of scavengers on Acid Red B degradation using CS, and (k) Photodegradation mechanism of Acid Red B dye removal using S-scheme $SrFeO_3$/g-C_3N_4 nanocomposite under UV light exposure, Reprinted with permission from Elsevier (License No. 5431310741717) (Hu *et al.,* 2022).

3.1.3. Phenols removal

Due to the extensive use of several synthetic compounds, organic micropollutants have widely been detected in several water bodies (König *et al.,* 2020; Sasi *et al.,* 2020). One of the harmful pollutants is phenols which harm the ecosystem even at very minute concentrations (ng L^{-1}~μg L^{-1}) (Mpatani *et al.,* 2021; Naveira *et al.,* 2021). Amongst phenolic compounds, bisphenol A (BPA) is a kind of endocrine disruptor generally utilized in various electronic tools, food storage vessels, water pipes, and remedial devices (Rodríguez-Llorente *et al.,* 2021; Xiao *et al.,* 2020), etc. To date, several works on S-scheme-based g-C_3N_4 nanocomposite for photocatalytic removal of phenolic compounds have been published. For instance, a novel peroxymonosulfate (PMS) assisted S-scheme $ZnFe_2O_4$/g-C_3N_4 (ZFO-CN) heterojunction photocatalyst was reported for the removal of BPA by Tang and coworkers (Tang *et al.,* 2022). The work reported the preparation of $ZnFe_2O_4$ (ZFO) from a spent alkaline Zn-Mn battery, which was further amalgamated with CN via a sol-gel method to form a ZFO-CN S-scheme heterostructure. The prepared photocatalyst has shown excellent photocatalytic ability in the presence of PMS against BPA due to extended visible light harnessing and the S-scheme charge transfer route. The PL and EIS results in Fig. 8a and b confirmed minimal recombination and efficient charge separation in the ZFO-CN nanocomposite. The BPA degradation results confirmed that Vis/ZFO-CN-0.5/PMS system has shown upto 97.7% removal efficacy within 60 min; however, 39.4% and 10.9% of BPA removal were observed for Vis/$ZnFe_2O_4$/PMS and Vis/CN/PMS photocatalytic systems, correspondingly (Fig. 8c). The formed S-scheme heterostructure increased the

redox ability and enhanced the charge separation and transferal ability among both ZFO and CN due to built-in IEF at the interface. The novel S-scheme photocatalytic degradation mechanism displayed shown in Fig. 8d presented Fermi levels (EF) of CN and ZFO before and after contact. After the contact amongst CN and ZFO photocatalysts, the IEF and band bending at the border of ZFO-CN resulted in the S-scheme charge transferal route beneath light illumination. The possible BPA S-scheme photocatalytic mechanism by Vis/ZFO-CN-0.5/PMS photocatalytic system was illustrated in Fig. 8d, showing the presence of $SO_4^{-\bullet}$, $^{\bullet}OH$, $^{\bullet}O_2^-$ radicals. At the same time, $^1O_2$ and h^+ non-radicals species were the leading oxidation species during the photodegradation process, which was confirmed through quenching tests. Another report on photocatalytic removal of BPA and NOR presented excellent photocatalytic ability using an S-scheme g-C_3N_4/$Bi_8(CrO_4)O_{11}$ (CN/BCO) nanocomposite (Gu *et al.*, 2022). Among all synthesized photocatalysts, hydrothermally prepared 10% CN/BCO nanocomposite exhibited upto 77% removal efficiency against both NOR and BPA pollutants within 45 min of visible light illumination, which was greater than the bare BCO and CN photocatalysts. The excellent photodegradation rate of S-scheme heterostructure was due to efficient charge separation and migration between the CN and BCO photocatalysts because, after the contact, there was IEF generation and band edge bending of the interface that enhanced the transference of photocarriers (established through photocurrent and EIS analysis as shown in Fig. 8e and f). The quenching experiments confirmed the major part of h^+ and $^{\bullet}O_2^-$ radicals during NOR and BPA photodegradation process. In addition, $^{\bullet}OH$ radicals also had minor role in degradation process. The possible S-scheme based photodegradation mechanism of CN/BCO heterojunction towards NOR and BPA was illustrated in Fig. 8g and h. Similarly, a work on visible light driven double S-scheme $Bi_7O_9I_3$/g-C_3N_4/Bi_3O_4Cl (BOI/GCN/BOCl) heterostructure was reported by Yuan and coworkers for phenol degradation (Yuan *et al.*, 2022). The ternary nanocomposite BOI/GCN/BOCl was synthesized using a simple oil bath method. Through EIS, photocurrent and PL experiments the lower recombination rate and higher charge separation efficacy was attained by BOI/GCN/BOCl-0.2 nanocomposite. Due to proficient charge separation efficacy, the BOI/GCN/BOCl-0.2 nanocomposite presented 100% removal efficiency while BOI/GCN/BOCl-0.1 and BOI/GCN/BOCl-0.3 nanocomposite had shown 84% and 95% degradation rate within 100 min of visible light exposure (Fig. 8i). Similarly, the attained TOC removal efficacy was lower than phenol removal efficacy i.e. 93.57% in 160 min of light exposure. Free radical scavenging experiments validated the important role of $^{\bullet}O_2^-$ and $^{\bullet}OH$ radicals which were the foremost oxidizing species during phenol degradation. The DFT studies also explored that a dual S-scheme charge immigration was formed at the interface of BOI, GCN and BOCl resulting in efficient photocarriers separation. To understand the dual S-scheme photocatalytic mechanism a proposed charge transfer mechanism was shown in Fig. 8j illustrating the energy level diagram and interface band bending with interfacial electron relocation among the three BOI, GCN and BOCl photocatalysts.

3.1.4. Heavy metal ion removal

Besides the presence of several organic pollutants, the occurrence of several heavy metals such as Cr(VI), Hg (II), Pb (II) and As(II) were also observed in water resources. The occurrence of heavy metals in water bodies has a hazardous effect on living organisms due to their carcinogenicity, strong toxicity and accumulation in organisms (Fu *et al.*, 2011; Hua *et al.*, 2012; Malik *et al.*, 2019). Hence, the removal of these pollutants is highly needed. To resolve this issue, several reports have been published on heavy metal ions removal. S-scheme based g-C_3N_4 heterostructures have also been synthesized to remove this harmful pollutant e.g. a novel S-scheme Au/g-C_3N_4/$BiO_{1.2}I_{0.6}$ plasmonic heterostructure was synthesized by calcination of mixture of BiOI (flower-like) and Au/g-C_3N_4 NSs which was then utilized for Cr(VI) reduction the bisphenol AF (BPAF) degradation (Dai *et al.*, 2022a). The visible light-assisted photocatalytic reaction explored that the optimized 4-Au/g-C_3N_4/$BiO_{1.2}I_{0.6}$ nanocomposite material has an apparent rate of 0.0174 min-1 and 0.0204 min-1 for BPAF degradation and Cr(VI) reduction, which was 6.5 and 3.7 folds higher than the bare g-C_3N_4, correspondingly. The observed BPAF removal efficacy of $BiO_{1.2}I_{0.6}$ and g-C_3N_4 was 10.8% and 33.0% within 150 min, individually (Fig. 9a). Similarly, for Cr(VI) reduction the observed degradation rate was 27.6% and 43.9% for $BiO_{1.2}I_{0.6}$ and g-C_3N_4 within 100 min (Fig. 9b). Amongst all synthesized

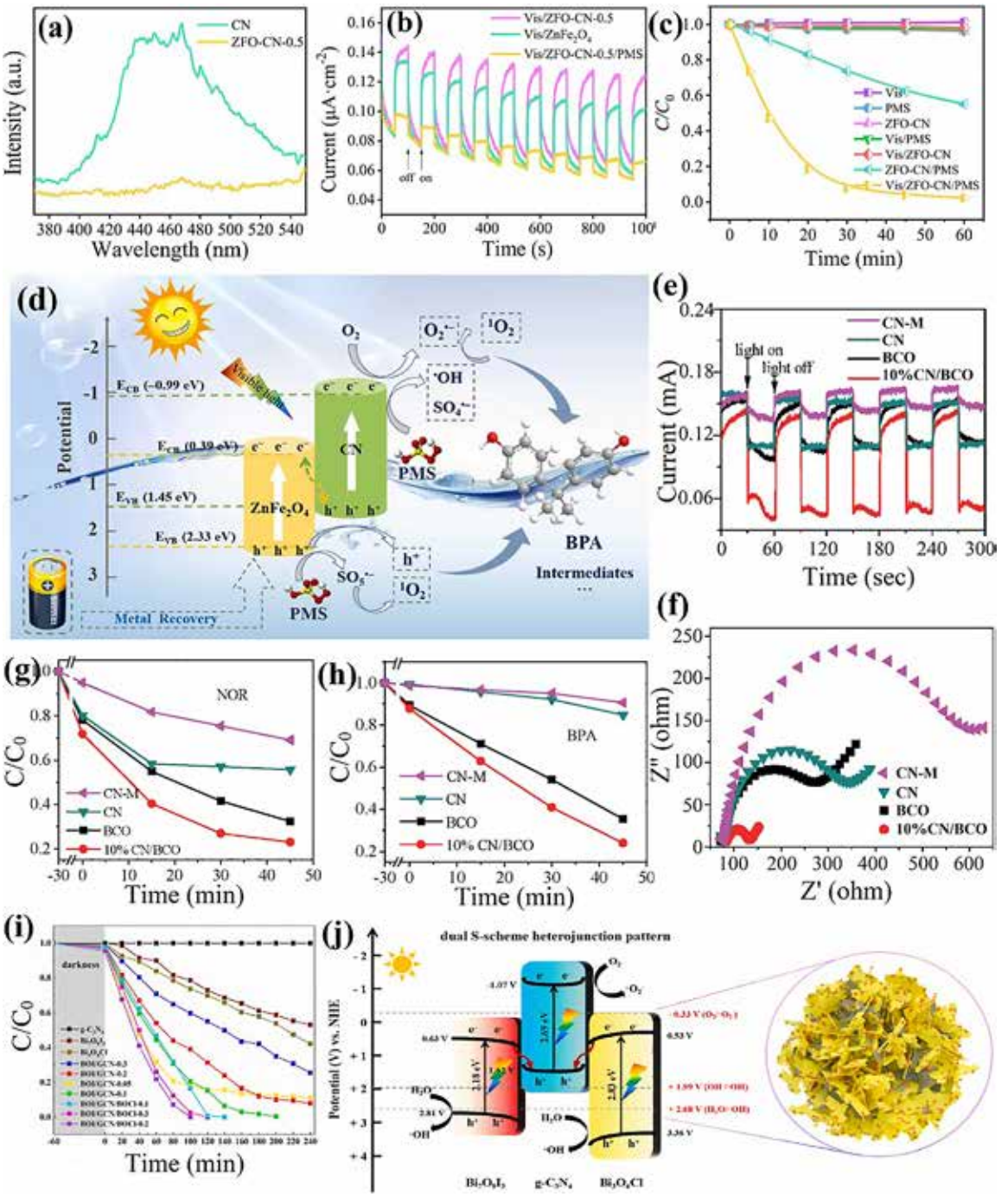

Figure 8. (a) PL spectra for CN and ZFO-CN-0.5 photocatalysts and (b) Photocurrent spectra with/without the addition of PMS, (c) BPA photodegradation under different reaction systems, (d) The probable BPA degradation mechanism using Vis/ZFO-CN-0.5/PMS photocatalytic system, Reprinted with permission from Elsevier (License No. 5431311068373) (Tang *et al.,* 2022). (e) Photocurrent, (f) EIS spectra, photodegradation curves of (g) NOR and (h) BPA using prepared CN-M, CN, BCO and 10% CN/BCO photocatalysts, Reprinted with permission from Elsevier (License No. 5431320344584) (Gu *et al.,* 2022). (i) Visible light-assisted photodegradation of phenol using g-C_3N_4, Bi_3O_4Cl, $Bi_7O_9I_3$, and BOI/GCN/BOCl nanocomposites, (j) Graphic illustration of possible charge transference in dual S-scheme BOI/GCN/BOCl nanocomposite, Reprinted with permission from Elsevier (License No. 5431320084241) (Yuan *et al.,* 2022).

photocatalysts, 4-Au/g-C_3N_4/$BiO_{1.2}I_{0.6}$ nanocomposite had shown superb photocatalytic ability towards BPAF removal and Cr(VI) photoreduction under visible light which was 91.8% and 87.3%, respectively. The incremented photocatalytic ability of nanocomposite ascribed to the LSPR (by Au NPs) and the S-scheme heterojunction formation, which enhanced charge carriers separation and transferal ability among both the g-C_3N_4 and $BiO_{1.2}I_{0.6}$ photocatalyst, validated through EIS analysis as shown in Fig. 9c. Graphic illustration of Au/g-C_3N_4/$BiO_{1.2}I_{0.6}$ nanocomposite was displayed in Fig. 9d presenting IEF generation-induced charge transmission and S-scheme heterojunction formation. Another heavy metal ion, i.e. uranium (VI) (U(VI)) reduction, was reported by Dai and his peer group (Dai *et al.*, 2021). They have reported a reduction of U(VI)) to U(IV) (insoluble tetravalent uranium) ion using S-scheme $ZnFe_2O_4$/g-C_3N_4 (ZFOCN) heterojunction photocatalyst which exhibited boosted light absorption ability and enhanced photoactivity. Through batch adsorption tests, the conquered adsorption ability (q_{max}) for U(VI) was 699.3 mg/g at pH 5.0 (Fig. 9e). Additionally, the ZFOCN-2 nanocomposite exhibited tremendous U(VI) photoreduction i.e. 1892.4 mg/g (adsorption + photoreduction) beneath visible LED light illumination with the degradation efficacy of 94.62% which was greater than physic-chemical adsorption. The enhanced photoreduction ability of ZFOCN corresponded to extended visible light garnering and a lower energy gap. During the photocatalytic process, firstly, the U(VI) get adsorbed on the ZFOCN surface and then after the adsorption process, it gets reduced to U(IV) under LED (visible light) illumination. The photocatalytic mechanism explored that after the contact between $ZnFe_2O_4$ and g-C_3N_4 photocatalysts, the $ZnFe_2O_4$ became positively charged and g-C_3N_4 negatively charged due to transferal of e^- and resulted in an electric field formation at the boundary. The proposed charge transferal route of U(VI) photoreduction was presented in Fig. 9f, demonstrating the substantial role of e^- and $^{\bullet}O_2^-$ radicals during the photoreduction process. Besides this, due to the magnetic property of the ZFOCN nanocomposite, the removal rate of U(VI) was affected by co-existing metal ions to some extent. Thus, after five recycles tests, the photoreduction rate decreased to 90%. Other work on Cr(VI) photoreduction was reported by Rajalakshmi *et al.* The work presented the preparation of S-scheme Ag_2CrO_4/g-C_3N_4 nanocomposite by a facile hydrothermal method (Rajalakshmi *et al.*, 2021). The photoactivity of the fabricated photocatalysts was examined towards Cr(VI) reduction and 2NP removal beneath visible light exposure. During the photodegradation experiments, the highest removal efficacy was attained for the optimized 10% Ag_2CrO_4 loaded g-C_3N_4 (ACCN10) photocatalysts towards 2NP degradation and Cr(VI) reduction compared to bare Ag_2CrO_4 and g-C_3N_4. The constructed S-scheme heterostructure speeded up the photocatalytic production by promoting redox ability, increasing light harvesting and assisting in charge separation and relocation (Fig. 9g).

3.2. Hydrogen evolution

The sense of urgency to find an alternative to depleting fossil fuels has been pressing for which the clean hydrogen gas (H_2) evolution via photocatalytic water splitting (PWS) has been regarded as a promising technology (Cao *et al.*, 2020; Lee, 2005; Maeda *et al.*, 2010). The PWS reaction is thermodynamically uphill, which needs at least bandgap energy of >1.23 eV to overcome the +237.2 kJ mol^{-1} of Gibbs free energy (Baniasadi *et al.*, 2013). To restrict the inevitable Coulombic attractions between like charges and inhibit recombination in traditional type-II and Z-scheme heterojunctions, it is well-evidenced that the S-scheme charge transfer route retains the effective charge carriers. To boost the S-scheme conception, Zhang *et al.* prepared Bi_2S_3/g-C_3N_4 binary S-scheme heterojunction via the solvothermal method (Zhang. *et al.*, 2021). The optimized loading of 0.6 % Bi_2S_3 (1D Nanorods) on 2D g-C_3N_4 nanosheets presented an exceptionally high H_2 production rate of 3394.1 µmolg/h, which was 2.6 folds greater than bare g-C_3N_4 (Fig. 10a and b). As shown in Fig. 10c, the Fermi level calculation confirmed S-scheme charge carrier migration of electrons from n-type oxidative Bi_2S_3 (0.55 V) to reductive g-C_3N_4 (-1.12 V) inducing IEF for preventing EHPs recombination. The conservation of reductive photogenerated electrons for H_2 production was reported by Yang *et al.* in Co_3O_4 quantum dots modified $CoTiO_3$/g-C_3N_4 ternary heterojunction (Yang *et al.*, 2022). The observed 1971.7 µmolg/h H_2 evolved within 5 h of irradiations which was attributed to synergistic effects of S-scheme charge carrier migration and electron acceptor co-catalytic property of Co_3O_4 quantum dots (Fig. 10f). Further, the consistent

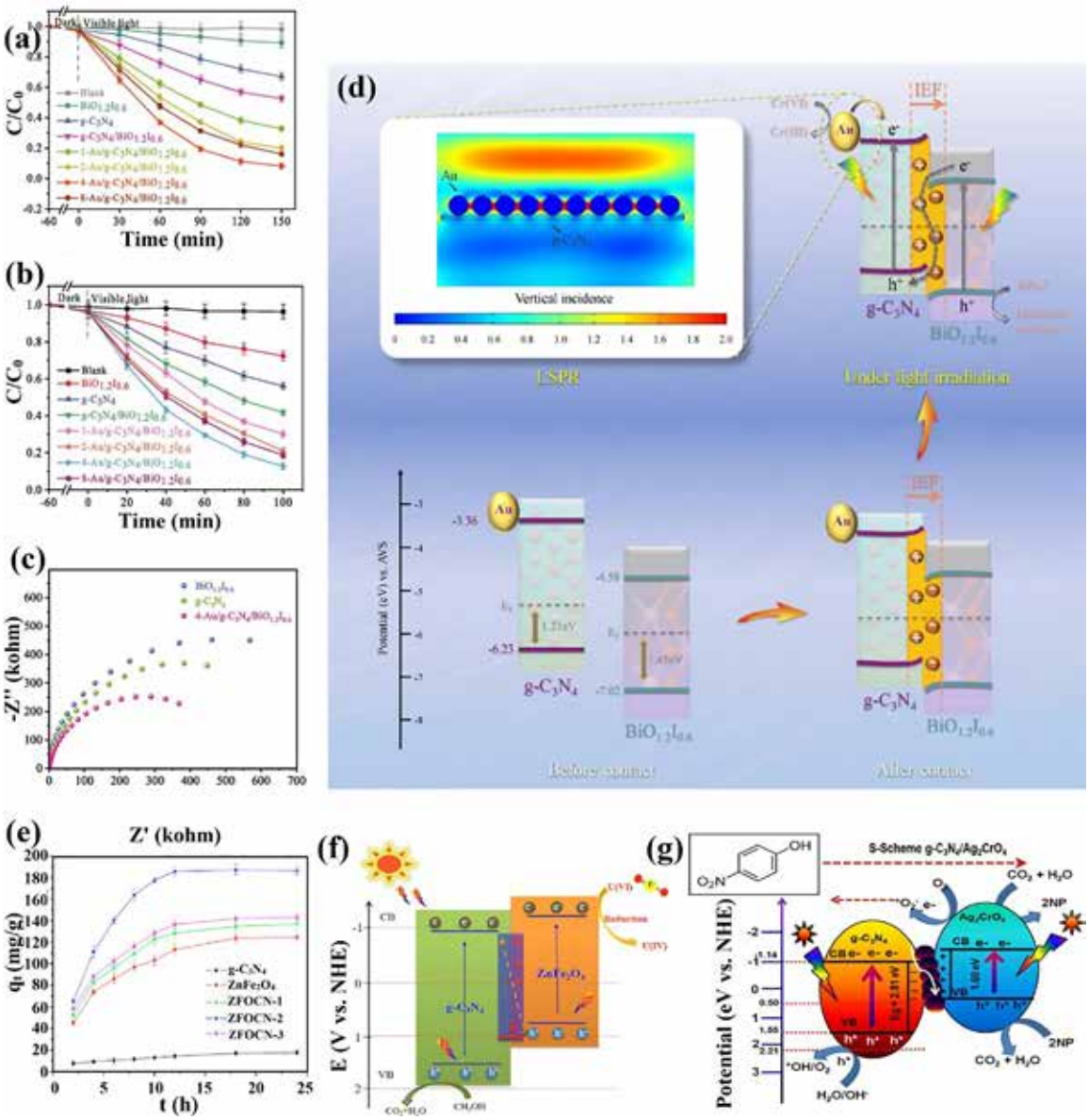

Figure 9. (a) BPAF photodegradation results, (b) Photocurrent and (c) EIS results of the fabricated photocatalysts, (d) Graphic sketch of S-scheme Au/g-C_3N_4/$BiO_{1.2}I_{0.6}$ photocatalytic system before contact and after contact as well as showing IEF generation and charge relocation beneath visible light exposure, Reprinted with permission from Elsevier (License No. 5433780470207) (Dai *et al.,* 2022a). (e) Influence of interacted time on U(VI) adsorption using g-C_3N_4, $ZnFe_2O_4$ and ZFOCN photocatalysts and (f) Representation of U(VI) photoreduction mechanism of ZFOCN-2 nanocomposite following S-scheme mechanism, Reprinted with permission from Elsevier (License No. 5431721196500) (Dai *et al.,* 2021). (g) The proposed S-scheme charge transfer route presenting electron transference in Ag_2CrO_4/g-C_3N_4 nanocomposite, Reprinted with permission from Elsevier (License No. 5431721336543) (Rajalakshmi *et al.,* 2021).

H_2 production rate was verified by the PL spectra and EIS Nyquist plots wherein minimum charge carrier recombination rate was obtained for Co_3O_4 quantum dots modified $CoTiO_3$/g-C_3N_4. Similarly, the co-catalytic effect of Ag nanospheres was exploited in g-C_3N_4/CdS S-scheme heterojunction, which showed high H_2O photoreduction efficacy of 204.19 µmolg/h H_2 generation (Shang *et al.*,

2022). The coupling of reduced graphene oxide (GO) with $NiFe_2O_4$-g-C_3N_4 S-scheme heterojunction exhibited a reduced bandgap from 2.75 to 2.48 eV with quenched PL intensity (Hafeez *et al.*, 2022). The resultant GO/$NiFe_2O_4$-g-C_3N_4 displayed 11,817 µmolg/h H_2 evolutions which were 76 times higher than $NiFe_2O_4$ NSs, as presented in Fig. 10d. The H_2 evolution mechanism in Fig. 10e represents the action of triethanolamine (TEOA) sacrificial agent which serves as holes scavengers to improve high reductive reaction and prevent charge carrier recombination which was also benefitted by built-in- IEF and band edge bending. Zhang *et al.* reported strategic synthesis for improved H_2 evolution wherein 254.4 µmolg/h and 12902.9 µmolg/h H_2 were produced after in-situ deposition and acid treatment of $NiTe_2$/g-C_3N_4 heterojunction, respectively (Fig. 10g) (Zhang *et al.*, 2022). The work claimed enhanced reactive sites and high hydrophilicity of photocatalyst after adding oleic acid, which was conducive to electron transference. The S-scheme mechanism notably improves the photocatalytic H_2 evolution rate provided minimal interfacial transfer resistance is present for high light absorption capacity (Fig. 10h).

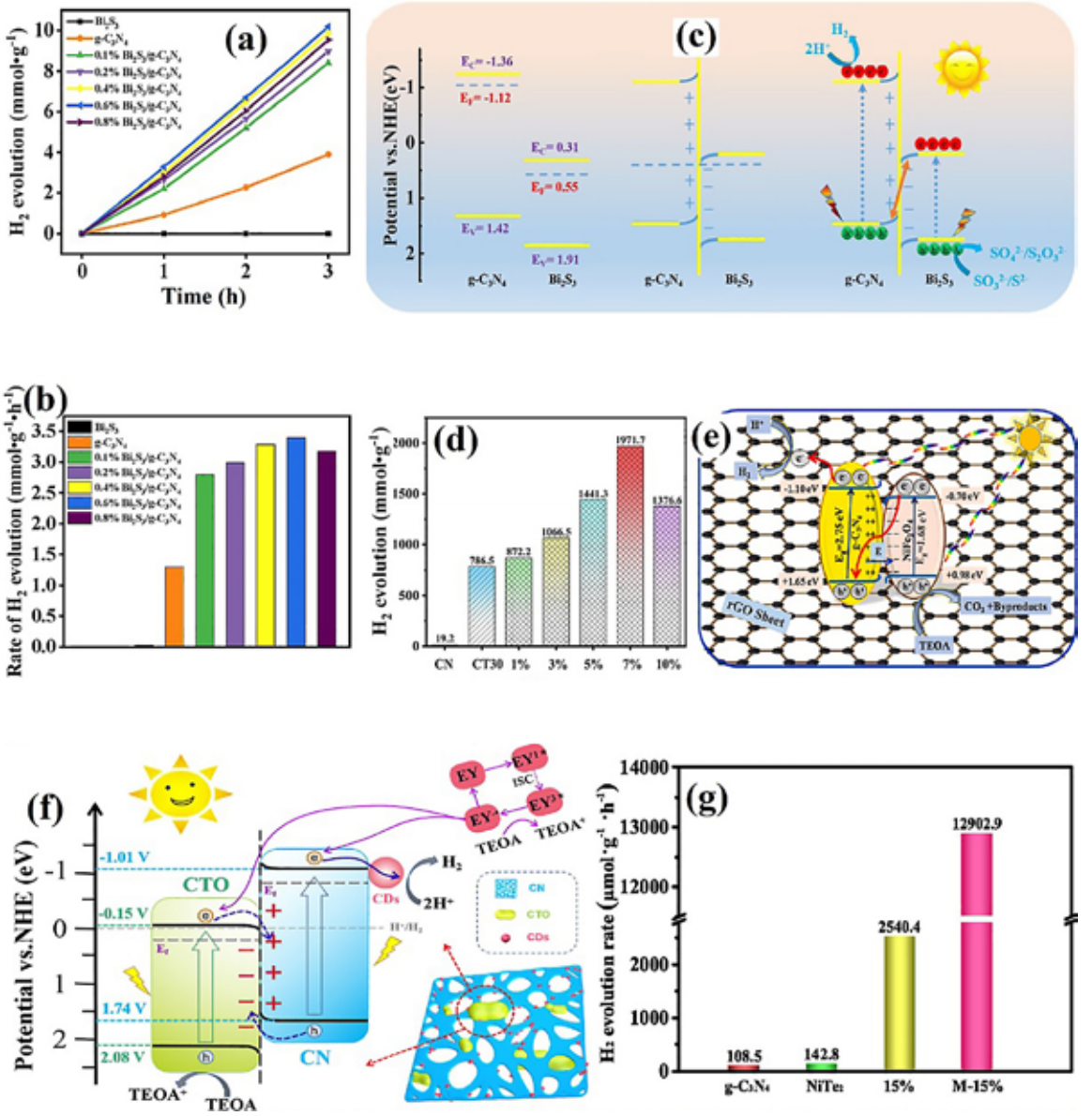

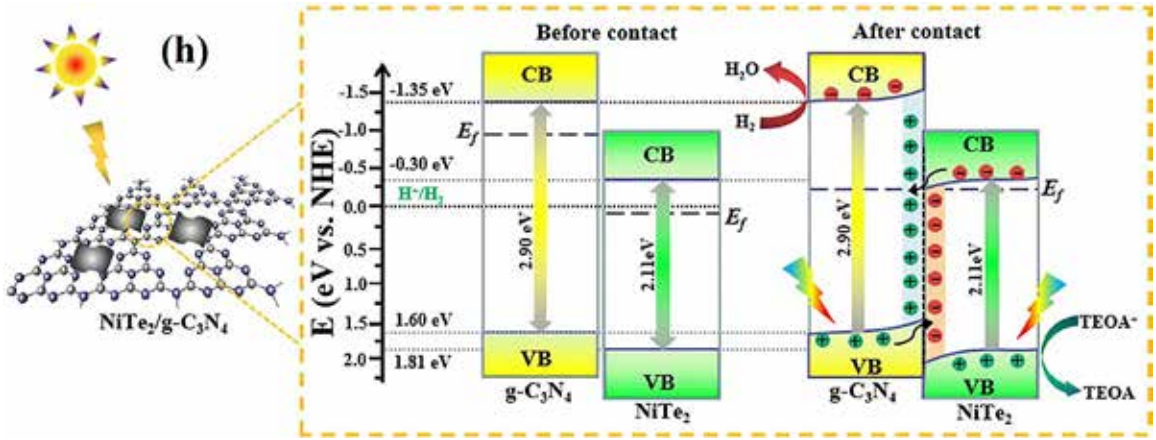

Figure 10. (a) Photocatalytic H_2 production results using Bi_2S_3/g-C_3N_4 nanocomposite, (b) Photocatalytic H_2 production rates of all synthesized photocatalysts, (c) Band gap alignments in Bi_2S_3 and g-C_3N_4 photocatalysts (before contact) and after contact presenting IEF formation and band edge bending at the border of Bi_2S_3/g-C_3N_4 leading to S-scheme charge migration route in Bi_2S_3/g-C_3N_4 beneath light exposure, Reprinted with permission from Elsevier (License No 5431730134202) (Zhang *et al.,* 2021). (d) Photocatalytic H_2 evolution rates of CN, CT30 and CTQx (x = QDs wt%) photocatalysts, (e) S-scheme charge migration mechanism of RNC-3 photocatalysts, Reprinted with permission from Elsevier (License No. 5431730809484). (f) Proposed S-scheme charge transferal route in CTQx photocatalyst, Reprinted with permission from Elsevier (License No. 5431730378154) (Yang *et al.,* 2022). (g) Photocatalytic H_2 production rates of different synthesized photocatalysts and (h) Proposed photocatalytic mechanism presenting efficient charge separation and transportation in $NiTe_2$/g-C_3N_4 S-scheme heterojunction, Reprinted with permission from Elsevier (License No. 5431730613334) (Zhang *et al.,* 2022).

3.3. CO_2 reduction

The inexplicable CO_2 emission in the atmosphere raises global warming concerns, instigating researchers to reduce CO_2 into high-value chemical feedstocks such as CO, CH_4, CH_3O_4, and other hydrocarbons (Ao *et al.*, 2020; Dey, 2007; Sahara *et al.*, 2015). The strategic conversion of solar energy into chemical energy paves the path for photocatalytic CO_2 reduction (Wu, J. *et al.*, 2017; Zhang S. *et al.*, 2020). However, the uphill reaction with a large thermodynamic barrier for CO_2 reduction requires high redox potentials of photocatalysts along with spatially separated electrons and holes for efficient CO_2 reduction (Ran *et al.*, 2018). Notably, the work function measurement is vital to exemplify the S-scheme charge carrier mechanism, as claimed by Qaraah *et al.* in the study of O-doped g-C_3N_4/N-doped Nb_2O_5. The highest charge separation in S-scheme heterostructure was proven through EIS analysis, as shown in (Fig. 11a). Wherein the calculated work function for N-doped Nb_2O_5 was 5.09 eV and 3.99 eV for O-doped g-C_3N_4 involving rapid electron transference from high Fermi level of O-doped g-C_3N_4 to N-doped Nb_2O_5 (Fig. 11e) (Qaraah *et al.*, 2022). Subsequently, the downward bend of N-doped Nb_2O_5 and upward bend of O-doped g-C_3N_4 contributes to high oxidative and reductive abilities (Fig. 11e). The EPR results presented in Fig. 11c and d show high-intensity EPR spectra for DMPO-$^{\cdot}$OH adduct for N-doped Nb_2O_5 whereas, an opposite trend is observed for DMPO-$^{\cdot}O_2^-$ as shown in. This is indicative that e^-, and h^+ remain intact in the CB of O-doped g-C_3N_4 and VB of N-doped Nb_2O_5 for an effective S-scheme charge migration over type-II (Fig. 11f). The apparent quantum efficiency of the optimized sample was 4.95% under the exposure of simulated sunlight radiation as shown in Fig. 11b. The work establishes a total CO_2 conversion rate of CO and CH_4 to be 6.04 and 6.19 times higher as compared to pristine O-doped g-C_3N_4 and N-doped Nb_2O_5, respectively. Similarly, Li *et al.* performed in-situ growth of $ZnIn_2S_4$ NSs on g-C_3N_4 tubes for the formation of intimate interface (Li *et al.*, 2022). Fig. 11g explains the S-scheme charge carrier migration with retention of high redox potential photogenerated electrons in $ZnIn_2S_4$ and oxidative holes in g-C_3N_4. The resultant $ZnIn_2S_4$/g-C_3N_4 S-scheme heterojunction possessed 833 µmolg/h CO production rates

at 420 nm that was 13 folds greater than pristine g-C_3N_4 (Fig. 11h). Apart from excellent S-scheme charge migration route, $ZnIn_2S_4$/g-C_3N_4 exhibited high BET specific surface area (137 cm^2/g) which increased the active sites for CO_2 adherence on photocatalyst surface. The CO_2 photoreduction activity was evaluated over Bi_3NbO_7/g-C_3N_4 heterostructure, which displayed high selectivity to the photocatalytic reduction of CO_2 to CH_4 (37.59 µmol g/h) with constant stability over 10 photocatalytic cycles (Wang *et al.*, 2022). The CO_2 reduction results were attributed to the decreased bandgap from 2.90 eV to 2.61 eV with extended visible light absorption up to 500 nm. In recent work, Mei *et al.* reported in-situ growth of CoO on porous g-C_3N_4 and formed a close equilibrium interface for S-scheme charge migration with high redox abilities (Mei *et al.*, 2021). The CoO/g-C_3N_4 composites exhibited a higher CO_2 reduction of 40.31 µmolg/h, whereas pristine CoO and g-C_3N_4 showed only 11.73 µmolg/h and 1.69 µmolg/h, respectively. The key target is to attain C2+ products by CO_2 conversion with high photostability and minimum charge carrier recombination.

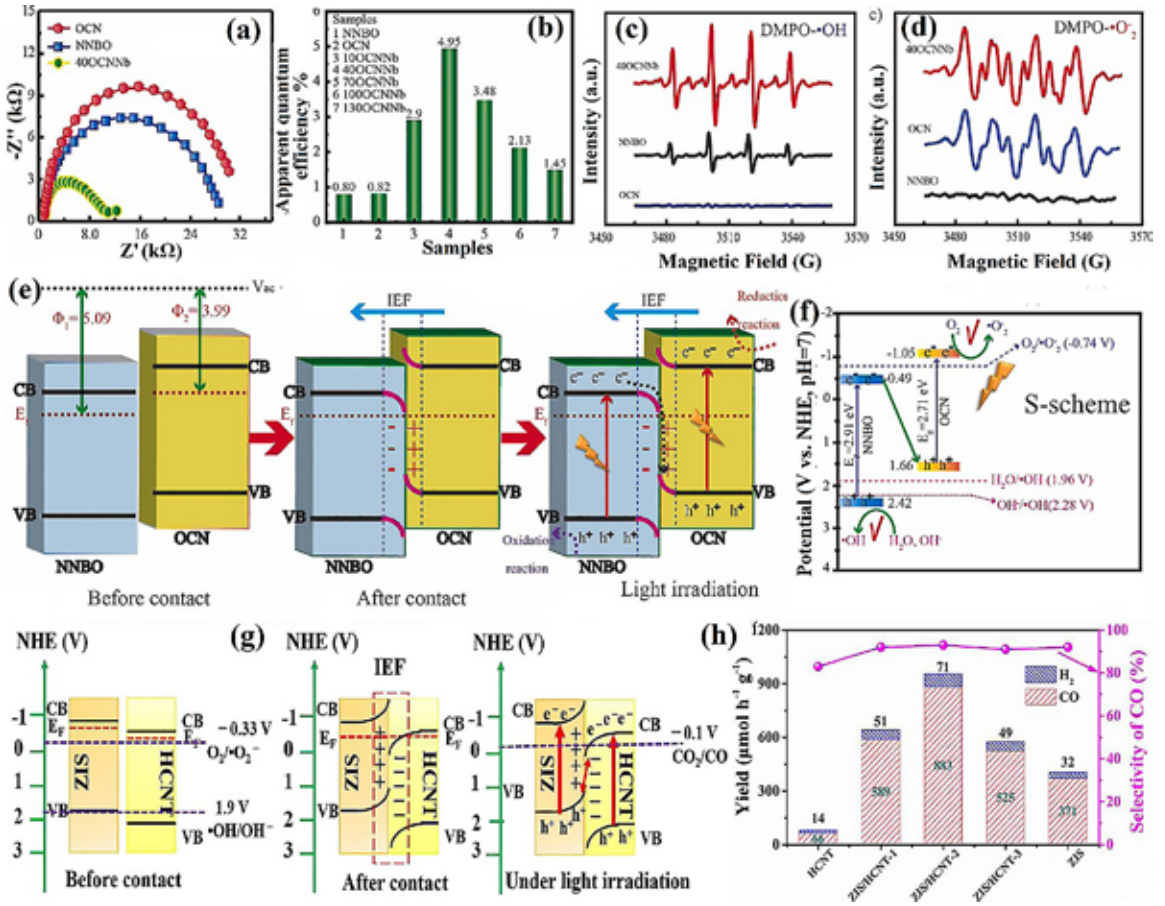

Figure 11. (a) EIS spectra of NNBO, OCN, and 40OCNNb nanocomposite, (b) AQE% for photocatalytic CO_2 reduction with H_2O using differently prepared photocatalysts, (c) DMPO-•OH and (d) DMPO-•O_2^- adducts (water solution and methanol solution, respectively) using NNBO, OCN, and 40OCNNb photocatalysts under 3 min of light irradiation, (e) Energy band alignments and band banding in NNBO and OCN before, after contact and in the presence of light presenting a generation of IEF and S-scheme charge migration, (f) Illustration of the S-scheme charge relocation path among NNBO and OCN photocatalysts for photocatalytic reaction, Reprinted with permission from Elsevier (License No. 5431731318945) (Qaraah *et al.*, 2022). (g) The photoreduction CO_2 and CO selectivity of the various fabricated photocatalysts, (h) Representation of energy band position of HCNT and ZIS before contact, after contact and S-scheme heterojunction photocatalytic system showing efficient charge migration in HCNT/ZIS for CO_2 reduction beneath light irradiation, Reprinted with permission from Elsevier (License No. 5431731503264) (Li *et al.*, 2022).

CONCLUSION

Recently, g-C_3N_4 has gained increasing interest as a prototype metal-free polymer photocatalyst due to its exemplary implementation in a broad range of tests. However, g-C_3N_4 photocatalytic effectiveness is still hindered by its restricted optical response range, the quick recombination rate of photoexcited charges, and poor oxidation ability. Fabrication of S-scheme derived g-C_3N_4 heterojunction using two or more SCs fully utilises their unique benefits to eliminate all of the limitations above instantaneously, depending on the features of different modification procedures. The focus on the areas of heterojunction, essential concepts of S-scheme, and fabrication methodologies of S-scheme-based g-C_3N_4 heterojunctions are all introduced in this study. Pollutants photodegradation, water splitting, photocatalytic disinfection, and CO_2 photoreduction into fuels are only some of the possible uses of S-scheme based g-C_3N_4 heterojunctions described in the last few years. S-scheme photocatalysts have a high driving force due to their high redox ability, which is made possible by the special charge carrier transfer mechanism. However, depending on the thermodynamic benefit of S-scheme photo-catalysts is not adequate since both reaction's thermodynamics and dynamics control the final photocatalytic performance. S-scheme photocatalysts may be made more effective in their photocatalytic roles via several different methods. (1) Modifying the RP and OP Fermi levels. Doping is a technique for modifying a semiconductor's Fermi level, and it may be used to increase the difference between the RP and OP Fermi levels. (2) The use of co-catalyst-facilitated change. It is well known that using an appropriate co-catalyst improves the photocarriers separation rate and reduces the barrier to photocatalytic activity. Consequently, it performs its function by loading the reduction cocatalyst onto the reduction photocatalyst surface and the oxidation cocatalyst onto the oxidation photocatalyst surface. (3) Regulating interfaces and engineering morphology. It is possible to boost the photocatalytic efficacy of S-scheme photocatalysts by carefully tailoring their morphological structure. For instance, the photoinduced charge carriers may be readily separated and dispersed on the surface of the photocatalyst for participation in the redox process because of the high contact area of 2D/2D composite structures.

Heterojunction photocatalysis has progressed long, but S-scheme heterojunction is only getting started. It would be very appreciated if you gave this some more thought and researched it more. First, a plausible photocatalyst for the target reaction may be designed with a thorough grasp of charge-transferal laws and the roles of the co-catalyst in S-scheme heterojunction. Second, it's essential to expand the use of S-scheme heterojunctions beyond their current niches in H_2O splitting, N_2 fixation, medicine, and selective chemical synthesis to make use of their benefits. We aim to get a molecular and atomic-level understanding of S-scheme photocatalysts using a mix of in-situ and ex-situ studies and theoretical modelling. Despite extensive research conducted over a few years, preparing S-scheme scheme-based g-C_3N_4 catalysts with the high photocatalytic ability and broad applicability remains difficult. Even further research is needed to understand the S-scheme mechanism fully.

Accordingly, more significant research into the charge transfer mechanism and reactions that occur in S-scheme heterojunctions is required. Therefore, the following are some doubts that need to be further researched and explained in the future: First, while many different approaches have been explored for creating an S-scheme based g-C_3N_4 photocatalyst, many of them require implementing extreme conditions with a complicated procedure, which increases the price of mass manufacturing. Therefore, in future studies, it will be necessary to closely monitor raw materials utilized in the synthesis of S-scheme based g-C_3N_4 photocatalyst to easier the fabrication processes and softer the reaction conditions, therefore decreasing the operational cost for synthesis. Second, additional in-situ characterization approaches should be broadly implemented into various S-scheme based g-C_3N_4 photocatalytic systems due to the extraordinary complexity of the photocarriers migration route in S-scheme heterojunction. The mechanisms of charge transference in an S-scheme-type heterojunction can be better understood with the help of these dependable in-situ characterization approaches. Third, it's essential to consider the heterojunction photocatalysts' stability. S-scheme heterojunctions, as is well known, are always made up of two or more semiconductor components joined together in some way (physical or chemical adsorption, electrostatic contact, etc.). The performance of g-C_3N_4-based heterojunctions degrades with time because the contact between the components

weakens during the photocatalytic reaction process. Therefore, more research into enhancing the interaction in g-C_3N_4-based heterojunction devices is necessary to ensure their long-term stability for real-world implementation. Finally, despite extensive research into the designing and fabricating effective S-scheme-based g-C_3N_4 photocatalysts, these materials' catalytic effectiveness still falls short of the requirements required for widespread commercial application. The maximum solar-to-H_2 conversion efficiency for H_2 generation using g-C_3N_4 is currently about 2%, which is still much below market norms of 10%. Therefore, additional research is needed to improve the photodegradation efficiency of g-C_3N_4-based photocatalysts. ♦

REFERENCES

Afroz, R., Masud, M. M., Akhtar, R., & Duasa, J. B. (2014). Water pollution: Challenges and future direction for water resource management policies in Malaysia. *Environment and urbanization ASIA*, *5*(1), 63-81.

Ahmad, F., Zhu, D., & Sun, J. (2021). Environmental fate of tetracycline antibiotics: degradation pathway mechanisms, challenges, and perspectives. *Environmental Sciences Europe*, *33*(1), 1-17.

Akhundi, A., Badiei, A., Ziarani, G. M., Habibi-Yangjeh, A., Munoz-Batista, M. J., & Luque, R. (2020). Graphitic carbon nitride-based photocatalysts: toward efficient organic transformation for value-added chemicals production. *Molecular Catalysis*, *488*, 110902.

Akhundi, A., Habibi-Yangjeh, A., Abitorabi, M., & Rahim Pouran, S. (2019). Review on photocatalytic conversion of carbon dioxide to value-added compounds and renewable fuels by graphitic carbon nitride-based photocatalysts. *Catalysis Reviews*, *61*(4), 595-628.

Akhundi, A., Zaker Moshfegh, A., Habibi-Yangjeh, A., & Sillanpää, M. (2022). Simultaneous Dual-Functional Photocatalysis by g-C_3N_4-Based Nanostructures. *ACS ES&T Engineering*, *2*(4), 564-585.

Alwin, E., Kočí, K., Wojcieszak, R., Zieliński, M., Edelmannová, M., & Pietrowski, M. (2020a). Influence of high temperature synthesis on the structure of graphitic carbon nitride and its hydrogen generation ability. *Materials*, *13*(12), 2756.

Alwin, E., Nowicki, W., Wojcieszak, R., Zieliński, M., & Pietrowski, M. (2020b). Elucidating the structure of the graphitic carbon nitride nanomaterials via X-ray photoelectron spectroscopy and X-ray powder diffraction techniques. *Dalton Transactions*, *49*(36), 12805-12813.

Ameta, R., Solanki, M. S., Benjamin, S., & Ameta, S. C. (2018). Photocatalysis. In *Advanced oxidation processes for waste water treatment* (pp. 135-175). Elsevier.

Amin, M., Shah, H. H., Fareed, A. G., Khan, W. U., Chung, E., Zia, A., Farooqi, Z. U. R., & Lee, C. (2022). Hydrogen production through renewable and non-renewable energy processes and their impact on climate change. *International Journal of Hydrogen Energy.*

Andersson, D. I. (2003). Persistence of antibiotic resistant bacteria. *Current opinion in microbiology*, *6*(5), 452-456.

Ao, C., Feng, B., Qian, S., Wang, L., Zhao, W., Zhai, Y., & Zhang, L. (2020). Theoretical study of transition metals supported on g-C_3N_4 as electrochemical catalysts for CO_2 reduction to CH_3OH and CH_4. *Journal of CO_2 Utilization*, *36*, 116-123.

Bai, J., Shen, R., Chen, W., Xie, J., Zhang, P., Jiang, Z., & Li, X. (2022). Enhanced photocatalytic H_2 evolution based on a Ti_3C_2/Zn_0. $7Cd_0$. $3S/Fe_2O_3$ Ohmic/S-scheme hybrid heterojunction with cascade 2D coupling interfaces. *Chemical Engineering Journal*, *429*, 132587.

Baniasadi, E., Dincer, I., & Naterer, G. (2013). Hybrid photocatalytic water splitting for an expanded range of the solar spectrum with cadmium sulfide and zinc sulfide catalysts. *Applied Catalysis A: General*, *455*, 25-31.

Bao, Y., Song, S., Yao, G., & Jiang, S. (2021). S-Scheme Photocatalytic Systems. *Solar RRL*, *5*(7), 2100118.

Bard, A. J. (1979). Photoelectrochemistry and heterogeneous photo-catalysis at semiconductors. *Journal of Photochemistry*, *10*(1), 59-75.

Bie, C., Cheng, B., Fan, J., Ho, W., & Yu, J. (2021a). Enhanced solar-to-chemical energy conversion of graphitic carbon nitride by two-dimensional cocatalysts. *EnergyChem*, *3*(2), 100051.

Bie, C., Yu, H., Cheng, B., Ho, W., Fan, J., & Yu, J. (2021b). Design, fabrication, and mechanism of nitrogen-doped graphene-based photocatalyst. *Advanced Materials*, *33*(9), 2003521.

Borthakur, S., & Saikia, L. (2019). $ZnFe_2O_4$@ g-C_3N_4 nanocomposites: An efficient catalyst for

Fenton-like photodegradation of environmentally pollutant Rhodamine B. *Journal of Environmental Chemical Engineering, 7*(2), 103035.

Brillas, E., & Martínez-Huitle, C. A. (2015). Decontamination of wastewaters containing synthetic organic dyes by electrochemical methods. An updated review. *Applied Catalysis B: Environmental, 166*, 603-643.

Cai, Z., Zhou, Y., Ma, S., Li, S., Yang, H., Zhao, S., Zhong, X., & Wu, W. (2017). Enhanced visible light photocatalytic performance of g-C_3N_4/CuS pn heterojunctions for degradation of organic dyes. *Journal of Photochemistry and Photobiology A: Chemistry, 348*, 168-178.

Cao, S., Low, J., Yu, J., & Jaroniec, M. (2015). Polymeric photocatalysts based on graphitic carbon nitride. *Advanced Materials, 27*(13), 2150-2176.

Cao, S., Piao, L., & Chen, X. (2020). Emerging photocatalysts for hydrogen evolution. *Trends in Chemistry, 2*(1), 57-70.

Cervantes-Avilés, P., & Keller, A. A. (2021). Incidence of metal-based nanoparticles in the conventional wastewater treatment process. *Water Research, 189*, 116603.

Chavoshani, A., Hashemi, M., Amin, M. M., & Ameta, S. C. (2020). Pharmaceuticals as emerging micropollutants. In *Micropollutants and Challenges: Emerging in the Aquatic Environments and Treatment Processes, 35*.

Chen, B., Lin, L., Fang, L., Yang, Y., Chen, E., Yuan, K., Zou, S., Wang, X., & Luan, T. (2018). Complex pollution of antibiotic resistance genes due to beta-lactam and aminoglycoside use in aquaculture arming. *Water Research, 134*, 200-208.

Chen, F., Liu, H., Bagwasi, S., Shen, X., & Zhang, J. (2010). Photocatalytic study of BiOCl for degradation of organic pollutants under UV irradiation. *Journal of Photochemistry and Photobiology A: Chemistry, 215*(1), 76-80.

Chen, H., & Wang, J. (2021). MOF-derived Co_3O_4-C@ FeOOH as an efficient catalyst for catalytic ozonation of norfloxacin. J*ournal of Hazardous Materials, 403*, 123697.

Chen, X., Zhang, J., Fu, X., Antonietti, M., & Wang, X. (2009). Fe-g-C_3N_4-catalyzed oxidation of benzene to phenol using hydrogen peroxide and visible light. *Journal of the American Chemical Society, 131*(33), 11658-11659.

Chen, Y., Gu, W., Tan, L., Ao, Z., An, T., & Wang, S. (2021). Photocatalytic H_2O_2 production using Ti_3C_2 MXene as a non-noble metal cocatalyst. *Applied Catalysis A: General, 618*, 118127.

Cheng, C., He, B., Fan, J., Cheng, B., Cao, S., & Yu, J. (2021). An inorganic/organic S-scheme heterojunction H_2-production photocatalyst and its charge transfer mechanism. *Advanced Materials, 33*(22), 2100317.

Cheng, L., Xiang, Q., Liao, Y., & Zhang, H. (2018). CdS-based photocatalysts. *Energy & Environmental Science, 11*(6), 1362-1391.

Cheng, L., Zhang, H., Li, X., Fan, J., & Xiang, Q. (2021). Carbon-graphitic carbon nitride hybrids for heterogeneous photocatalysis. *Small, 17*(1), 2005231.

Crini, G., & Lichtfouse, E. (2019). Advantages and disadvantages of techniques used for wastewater treatment. *Environmental Chemistry Letters, 17*(1), 145-155.

Dai, B., Chen, X., Yang, X., Yang, G., Li, S., Zhang, L., Mu, F., Zhao, W., & Leung, D. Y. (2022a). Designing S-scheme Au/g-C_3N_4/BiO1. 2I0. 6 plasmonic heterojunction for efficient visible-light photocatalysis. *Separation and Purification Technology, 287,* 120531.

Dai, B., Zhao, W., Wei, W., Cao, J., Yang, G., Li, S., Sun, C., & Leung, D. Y. (2022b). Photocatalytic reduction of CO_2 and degradation of Bisphenol-S by g-C_3N_4/Cu_2O@Cu S-scheme heterojunction: Study on the photocatalytic performance and mechanism insight. *Carbon, 193*, 272-284.

Dai, Z., Zhen, Y., Sun, Y., Li, L., & Ding, D. (2021). $ZnFe_2O_4$/g-C_3N_4 S-scheme photocatalyst with enhanced adsorption and photocatalytic activity for uranium (VI) removal. *Chemical Engineering Journal, 415*, 129002.

Davies, K. R., Cherif, Y., Pazhani, G. P., Anantharaj, S., Azzi, H., Terashima, C., Fujishima, A., & Pitchaimuthu, S. (2021). The upsurge of photocatalysts in antibiotic micropollutants treatment: Materials design, recovery, toxicity and bioanalysis. *Journal of photochemistry and photobiology C: Photochemistry Reviews, 48*, 100437.

Deng, X., Wang, D., Li, H., Jiang, W., Zhou, T., Wen, Y., Yu, B., Che, G., & Wang, L. (2022). Boosting interfacial charge separation and photocatalytic activity of 2D/2D g-C_3N_4/$ZnIn_2S_4$ S-scheme heterojunction under visible light irradiation. *Journal of Alloys and Compounds, 894*, 162209.

Dey, G. (2007). Chemical reduction of CO_2 to different products during photo catalytic reaction on TiO_2 under diverse conditions: an overview. *Journal of Natural Gas Chemistry,* 16(3), 217-226.

Diao, W., He, J., Wang, Q., Rao, X., & Zhang, Y. (2021). K, Na and Cl co-doped TiO_2 nanorod arrays on carbon cloth for efficient photocatalytic degradation of formaldehyde under UV/visible LED irradiation. *Catalysis Science & Technology, 11*(1), 230-238.

Du, J., Zhao, H., Liu, S., Xie, H., Wang, Y., & Chen, J. (2017). Antibiotics in the coastal water of the South Yellow Sea in China: occurrence, distribution and ecological risks. *Science of The Total Environment, 595*, 521-527.

Freeman, H., Harten, T., Springer, J., Randall, P., Curran, M. A., & Stone, K. (1992). Industrial pollution prevention! A critical review. Journal of the Air & Waste *Management Association, 42*(5), 618-656.

Fu, F., & Wang, Q. (2011). Removal of heavy metal ions from wastewaters: a review. *Journal of environmental management, 92*(3), 407-418.

Fu, J., Xu, Q., Low, J., Jiang, C., & Yu, J. (2019). Ultrathin 2D/2D WO_3/g-C_3N_4 step-scheme H_2-production photocatalyst. *Applied Catalysis B: Environmental, 243*, 556-565.

Fu, J., Yu, J., Jiang, C., & Cheng, B. (2018). g-C_3N_4-Based heterostructured photocatalysts. *Advanced Energy Materials, 8*(3), 1701503.

Ge, H., Xu, F., Cheng, B., Yu, J., & Ho, W. (2019). S-scheme heterojunction TiO_2/CdS nanocomposite nanofiber as H_2-production photocatalyst. *ChemCatChem, 11*(24), 6301-6309.

González-Pleiter, M., Gonzalo, S., Rodea-Palomares, I., Leganés, F., Rosal, R., Boltes, K., Marco, E., & Fernández-Piñas, F. (2013). Toxicity of five antibiotics and their mixtures towards photosynthetic aquatic organisms: implications for environmental risk assessment. *Water Research, 47*(6), 2050-2064.

Gordanshekan, A., Arabian, S., Nazar, A. R. S., Farhadian, M., & Tangestaninejad, S. (2023). A comprehensive comparison of green Bi_2WO_6/g-C_3N_4 and Bi_2WO_6/TiO_2 S-scheme heterojunctions for photocatalytic adsorption/degradation of Cefixime: Artificial neural network, degradation pathway, and toxicity estimation. *Chemical Engineering Journal, 451*, 139067.

Gu, X., Chen, T., Lei, J., Yang, Y., Zheng, X., Zhang, S., Zhu, Q., Fu, X., Meng, S., & Chen, S. (2022). Self-assembly synthesis of S-scheme g-C_3N_4/Bi_8 (CrO_4) O_{11} for photocatalytic degradation of norfloxacin and bisphenol A. *Chinese Journal of Catalysis, 43*(10), 2569-2580.

Gu, X., Li, C., Yuan, S., Ma, M., Qiang, Y., & Zhu, J. (2016). ZnO based heterojunctions and their application in environmental photocatalysis. *Nanotechnology, 27*(40), 402001.

Guo, Q., Zhou, C., Ma, Z., & Yang, X. (2019). Fundamentals of TiO_2 photocatalysis: concepts, mechanisms, and challenges. *Advanced Materials, 31*(50), 1901997.

Gupta, S., Mittal, Y., Panja, R., Prajapati, K. B., & Yadav, A. K. (2021). Conventional wastewater treatment technologies. *Current Developments in Biotechnology and Bioengineering*, 47-75.

Hafeez, H. Y., Mohammed, J., Ndikilar, C. E., Suleiman, A. B., Sa'id, R. S., & Muhammad, I. (2022). Synergistic utilization of magnetic rGO/$NiFe_2O_4$-g-C_3N_4 S-Scheme heterostructure photocatalyst with enhanced charge carrier separation and transfer: A highly stable and robust photocatalyst for efficient solar fuel (hydrogen) generation. *Ceramics International.*

He, F., Zhu, B., Cheng, B., Yu, J., Ho, W., & Macyk, W. (2020). 2D/2D/0D TiO_2/C_3N_4/Ti_3C_2 MXene composite S-scheme photocatalyst with enhanced CO_2 reduction activity. *Applied Catalysis B: Environmental, 272*, 119006.

He, Y., Wang, Y., Zhang, L., Teng, B., & Fan, M. (2015). High-efficiency conversion of CO_2 to fuel over ZnO/g-C_3N_4 photocatalyst. *Applied Catalysis B: Environmental, 168*, 1-8.

Hou, H., & Zhang, X. (2020). Rational design of 1D/2D heterostructured photocatalyst for energy and environmental applications. *Chemical Engineering Journal, 395*, 125030.

Hu, S., Yuan, J., Tang, S., Luo, D., Shen, Q., Qin, Y., Zhou, J., Tang, Q., Chen, S., & Luo, X. (2022). Perovskite-type $SrFeO_3$/g-C_3N_4 S-scheme photocatalyst for enhanced degradation of Acid Red B. *Optical Materials, 132*, 112760.

Hu, X., & Hu, C. (2007). Preparation and visible-light photocatalytic activity of Ag_3VO_4 powders. *Journal of Solid State Chemistry, 180*(2), 725-732.

Hua, M., Zhang, S., Pan, B., Zhang, W., Lv, L., & Zhang, Q. (2012). Heavy metal removal from water/wastewater by nanosized metal oxides: a review. *Journal of Hazardous Materials, 211*, 317-331.

Huang, H., Liu, C., Ou, H., Ma, T., & Zhang, Y. (2019). Self-sacrifice transformation for fabrication of type-I and type-II heterojunctions in hierarchical BixOyIz/g-C_3N_4 for efficient visible-light photocatalysis. *Applied Surface Science, 470*, 1101-1110.

Iwuozor, K. O., Abdullahi, T. A., Ogunfowora, L. A., Emenike, E. C., Oyekunle, I. P., Gbadamosi, F. A., & Ighalo, J. O. (2021). Mitigation of levofloxacin from aqueous media by adsorption: a review. *Sustainable Water Resources Management*, *7*(6), 1-18.

Khachatourians, G. G. (1998). Agricultural use of antibiotics and the evolution and transfer of antibiotic-resistant bacteria. *Cmaj, 159*(9), 1129-1136.

König, R., Spaggiari, M., Santoliquido, O., Principi, P., Bianchi, G., & Ortona, A. (2020). Micropollutant adsorption from water with engineered porous ceramic architectures produced by additive manufacturing and coated with natural zeolite. *Journal of Cleaner Production, 258*, 120500.

Kudo, A., Ueda, K., Kato, H., & Mikami, I. (1998). Photocatalytic O_2 evolution under visible light irradiation on $BiVO_4$ in aqueous $AgNO_3$ solution. *Catalysis Letters*, *53*(3), 229-230.

Kumar, A. (2022). Impact of Textile Wastewater on Water Quality. *Central Asian Journal of Medical and Natural Science*, *3*(3), 449-459.

Kumar, R., Sudhaik, A., Khan, A. A. P., Raizada, P., Asiri, A. M., Mohapatra, S., Thakur, S., Thakur, V. K., & Singh, P. (2021). Current status on designing of dual Z-scheme photocatalysts for energy and environmental applications. *Journal of Industrial and Engineering Chemistry.*

Kumar, S., Karthikeyan, S., & Lee, A. F. (2018). g-C_3N_4-based nanomaterials for visible light-driven photocatalysis. *Catalysts*, *8*(2), 74.

Kumari, P., Bahadur, N., Kong, L., O'Dell, L. A., Merenda, A., & Dumee, L. (2022). Engineering Schottky-like and heterojunction material for enhanced photocatalysis performance-a review. *Materials Advances*.

Lee, J. S. (2005). Photocatalytic water splitting under visible light with particulate semiconductor catalysts. *Catalysis Surveys from Asia*, *9*(4), 217-227.

Lellis, B., Fávaro-Polonio, C. Z., Pamphile, J. A., & Polonio, J. C. (2019). Effects of textile dyes on health and the environment and bioremediation potential of living organisms. *Biotechnology Research and Innovation*, *3*(2), 275-290.

Li, B., Zhang, B., Zhang, Y., Zhang, M., Huang, W., Yu, C., Sun, J., Feng, J., Dong, S., & Sun, J. (2021). Porous g-C_3N_4/TiO_2 S-scheme heterojunction photocatalyst for visible-light driven H_2-production and simultaneous wastewater purification. *International Journal of Hydrogen Energy*, *46*(64), 32413-32424.

Li, J., See, K. F., & Chi, J. (2019). Water resources and water pollution emissions in China's industrial sector: A green-biased technological progress analysis. *Journal of Cleaner Production*, *229*, 1412-1426.

Li, L., Ma, D., Xu, Q., & Huang, S. (2022). Constructing hierarchical $ZnIn_2S_4$/g-C_3N_4 S-scheme heterojunction for boosted CO_2 photoreduction performance. *Chemical Engineering Journal*, *437*, 135153.

Li, Q., Zhao, W., Zhai, Z., Ren, K., Wang, T., Guan, H., & Shi, H. (2020). 2D/2D Bi_2MoO_6/g-C_3N_4 S-scheme heterojunction photocatalyst with enhanced visible-light activity by Au loading. *Journal of Materials Science & Technology*, *56*, 216-226.

Li, X., Garlisi, C., Guan, Q., Anwer, S., Al-Ali, K., Palmisano, G., & Zheng, L. (2021). A review of material aspects in developing direct Z-scheme photocatalysts. *Materials Today*, *47*, 75-107.

Li, Y., Jin, R., Xing, Y., Li, J., Song, S., Liu, X., Li, M., & Jin, R. (2016). Macroscopic foam-like holey ultrathin g-C_3N_4 nanosheets for drastic improvement of visible-light photocatalytic activity. *Advanced Energy Materials*, *6*(24), 1601273.

Li, Y., Li, X., Zhang, H., Fan, J., & Xiang, Q. (2020). Design and application of active sites in g-C_3N_4-based photocatalysts. *Journal of Materials Science & Technology*, *56*, 69-88.

Li, Y., Meng, J., Zhu, Y., Yang, Y., Zhang, X., & Zheng, X. (2022). Ultrafine Ru nanoparticles confined in graphene-doped porous g-C_3N_4 for effectively boosting ammonia borane hydrolysis. *Colloids and Surfaces A: Physicochemical and Engineering Aspects*, *649*, 129513.

Li, Y., Wang, G., Zhang, H., Qian, W., Li, D., Guo, Z., Zhou, R., & Xu, J. (2022). Hierarchical flower-like 0D/3D g-C_3N_4/TiO_2 S-scheme heterojunction with enhanced photocatalytic activity. *Colloids and Surfaces A: Physicochemical and Engineering Aspects*, *646*, 128942.

Li, Y., Xia, Z., Yang, Q., Wang, L., & Xing, Y. (2022). Review on g-C_3N_4-based S-scheme Heterojunction Photocatalysts. *Journal of Materials Science & Technology.*

Li, Y., Zhang, M., Zhou, L., Yang, S., Wu, Z., & Ma, Y. (2021). Recent Advances in Surface-Modified g-C_3N_4-Based Photocatalysts for H-2 Production and CO_2 Reduction. *Acta Physico-Chimica Sinica*, *37*(6).

Li, Y., Zhou, M., Cheng, B., & Shao, Y. (2020). Recent advances in g-C_3N_4-based heterojunction photocatalysts. *Journal of Materials Science & Technology, 56*, 1-17.

Li, Z., Meng, X., & Zhang, Z. (2018). Recent development on MoS2-based photocatalysis: A review. *Journal of photochemistry and photobiology C: Photochemistry Reviews, 35*, 39-55.

Lian, X., Xue, W., Dong, S., Liu, E., Li, H., & Xu, K. (2021). Construction of S-scheme Bi_2WO_6/g-C_3N_4 heterostructure nanosheets with enhanced visible-light photocatalytic degradation for ammonium dinitramide. *Journal of Hazardous Materials, 412*, 125217.

Liao, G., Gong, Y., Zhang, L., Gao, H., Yang, G.-J., & Fang, B. (2019). Semiconductor polymeric graphitic carbon nitride photocatalysts: the "holy grail" for the photocatalytic hydrogen evolution reaction under visible light. *Energy & Environmental Science, 12*(7), 2080-2147.

Liu, D., Chen, S., Li, R., & Peng, T. (2021). Review of Z-scheme heterojunctions for photocatalytic energy conversion. *Acta Phys.-Chim. Sin, 37*, 2010017.

Liu, J., Ma, N., Wu, W., & He, Q. (2020). Recent progress on photocatalytic heterostructures with full solar spectral responses. *Chemical Engineering Journal, 393*, 124719.

Liu, J., Wei, X., Sun, W., Guan, X., Zheng, X., & Li, J. (2021). Fabrication of S-scheme CdS-g-C_3N_4-graphene aerogel heterojunction for enhanced visible light driven photocatalysis. *Environmental Research, 197*, 111136.

Liu, X., Ma, R., Zhuang, L., Hu, B., Chen, J., Liu, X., & Wang, X. (2021). Recent developments of doped g-C_3N_4 photocatalysts for the degradation of organic pollutants. *Critical Reviews in Environmental Science and Technology, 51*(8), 751-790.

Low, J., Jiang, C., Cheng, B., Wageh, S., Al-Ghamdi, A. A., & Yu, J. (2017a). A review of direct Z-scheme photocatalysts. *Small Methods, 1*(5), 1700080.

Low, J., Yu, J., Jaroniec, M., Wageh, S., & Al-Ghamdi, A. A. (2017b). Heterojunction photocatalysts. *Advanced Materials, 29*(20), 1601694.

Lu, Z., & Wang, Z. (2023). S-scheme $CuWO_4$@g-C_3N_4 core-shell microsphere for CO_2 photoreduction. *Materials Science in Semiconductor Processing, 153*, 107177.

Maeda, K., & Domen, K. (2010). Photocatalytic water splitting: recent progress and future challenges. *The Journal of Physical Chemistry Letters, 1*(18), 2655-2661.

Maheshwari, K., Agrawal, M., & Gupta, A. (2021). Dye Pollution in Water and Wastewater. In *Novel Materials for Dye-containing Wastewater Treatment* (pp. 1-25). Springer.

Maihemllti, M., Okitsu, K., Talifur, D., Tursun, Y., & Abulizi, A. (2021). In situ self-assembled S-scheme BiOBr/pCN hybrid with enhanced photocatalytic activity for organic pollutant degradation and CO_2 reduction. *Applied Surface Science, 556*, 149828.

Malik, L. A., Bashir, A., Qureashi, A., & Pandith, A. H. (2019). Detection and removal of heavy metal ions: a review. *Environmental Chemistry Letters, 17*(4), 1495-1521.

Mani, S., Chowdhary, P., & Bharagava, R. N. (2019). Textile wastewater dyes: toxicity profile and treatment approaches. In *Emerging and eco-friendly approaches for waste management* (pp. 219-244). Springer.

Mei, F., Zhang, J., Liang, C., & Dai, K. (2021). Fabrication of novel CoO/porous graphitic carbon nitride S-scheme heterojunction for efficient CO_2 photoreduction. *Materials Letters, 282*, 128722.

Meng, A., Zhou, S., Wen, D., Han, P., & Su, Y. (2022). g-C_3N_4/$CoTiO_3$ S-scheme heterojunction for enhanced visible light hydrogen production through photocatalytic pure water splitting. *Chinese Journal of Catalysis, 43*(10), 2548-2557.

Meng, S., Zhang, J., Chen, S., Zhang, S., & Huang, W. (2019). Perspective on construction of heterojunction photocatalysts and the complete utilization of photogenerated charge carriers. *Applied Surface Science, 476*, 982-992.

Mishra, M., & Chun, D.-M. (2015). α-Fe_2O_3 as a photocatalytic material: A review. *Applied Catalysis A: General, 498*, 126-141.

Mpatani, F. M., Han, R., Aryee, A. A., Kani, A. N., Li, Z., & Qu, L. (2021). Adsorption performance of modified agricultural waste materials for removal of emerging micro-contaminant bisphenol A: a comprehensive review. *Science of The Total Environment, 780*, 146629.

Naveira, C., Rodrigues, N., Santos, F. S., Santos, L. N., & Neves, R. A. (2021). Acute toxicity of Bisphenol A (BPA) to tropical marine and estuarine species from different trophic groups. *Environmental Pollution, 268*, 115911.

Nguyen, T. D., Nguyen, V.-H., Nanda, S., Vo, D.-V. N., Nguyen, V. H., Van Tran, T., Nong, L. X., Nguyen,

T. T., Bach, L.-G., & Abdullah, B. (2020). $BiVO_4$ photocatalysis design and applications to oxygen production and degradation of organic compounds: a review. *Environmental Chemistry Letters, 18*(6), 1779-1801.

Niu, J., Ding, S., Zhang, L., Zhao, J., & Feng, C. (2013). Visible-light-mediated Sr-Bi_2O_3 photocatalysis of tetracycline: kinetics, mechanisms and toxicity assessment. *Chemosphere, 93*(1), 1-8.

Niu, P., Pan, Z., Wang, S., & Wang, X. (2021). Cobalt Phosphide Cocatalysts Coated with Porous N-doped Carbon Layers for Photocatalytic CO_2 Reduction. *ChemCatChem, 13*(16), 3581-3587.

Patel, M., Kumar, R., Kishor, K., Mlsna, T., Pittman Jr, C. U., & Mohan, D. (2019). Pharmaceuticals of emerging concern in aquatic systems: chemistry, occurrence, effects, and removal methods. *Chemical reviews, 119*(6), 3510-3673.

Paul, T., Das, D., Das, B. K., Sarkar, S., Maiti, S., & Chattopadhyay, K. K. (2019). CsPbBrCl2/g-C_3N_4 type II heterojunction as efficient visible range photocatalyst. *Journal of Hazardous Materials, 380,* 120855.

Pirhashemi, M., Habibi-Yangjeh, A., & Pouran, S. R. (2018). Review on the criteria anticipated for the fabrication of highly efficient ZnO-based visible-light-driven photocatalysts. *Journal of Industrial and Engineering Chemistry, 62,* 1-25.

Preeyanghaa, M., Vinesh, V., & Neppolian, B. (2022). Construction of S-scheme 1D/2D rod-like g-C_3N_4/V_2O_5 heterostructure with enhanced sonophotocatalytic degradation for Tetracycline antibiotics. *Chemosphere, 287,* 132380.

Qaraah, F. A., Mahyoub, S. A., Hezam, A., Qaraah, A., Xin, F., & Xiu, G. (2022). Synergistic effect of hierarchical structure and S-scheme heterojunction over O-doped g-C_3N_4/N-doped Nb_2O_5 for highly efficient Photocatalytic CO_2 Reduction. *Applied Catalysis B: Environmental*, 121585.

Qiao, M., Ying, G.-G., Singer, A. C., & Zhu, Y.-G. (2018). Review of antibiotic resistance in China and its environment. *Environment international,* 110, 160-172.

Rajalakshmi, N., Barathi, D., Meyvel, S., & Sathya, P. (2021). S-scheme Ag_2CrO_4/g-C_3N_4 photocatalyst for effective degradation of organic pollutants under visible light. *Inorganic Chemistry Communications, 132,* 108849.

Ran, J., Jaroniec, M., & Qiao, S. Z. (2018). Cocatalysts in semiconductor-based photocatalytic CO_2 reduction: achievements, challenges, and opportunities. *Advanced Materials, 30*(7), 1704649.

Reddy, P. A. K., Reddy, P. V. L., Kwon, E., Kim, K.-H., Akter, T., & Kalagara, S. (2016). Recent advances in photocatalytic treatment of pollutants in aqueous media. *Environment international, 91,* 94-103.

Ren, Y., Zeng, D., & Ong, W.-J. (2019). Interfacial engineering of graphitic carbon nitride (g-C_3N_4)-based metal sulfide heterojunction photocatalysts for energy conversion: a review. *Chinese journal of catalysis, 40*(3), 289-319.

Rodríguez-Llorente, D., Navarro, P., Santiago, R., Águeda, V. I., Álvarez-Torrellas, S., García, J., & Larriba, M. (2021). Extractive removal and recovery of bisphenol A from aqueous solutions using terpenoids and hydrophobic eutectic solvents. *Journal of Environmental Chemical Engineering, 9*(5), 106128.

Sabri, M., Habibi-Yangjeh, A., Rahim Pouran, S., & Wang, C. (2021). Titania-activated persulfate for environmental remediation: the-state-of-the-art. *Catalysis Reviews,* 1-56.

Sah, C.-T., Noyce, R. N., & Shockley, W. (1957). Carrier generation and recombination in pn junctions and pn junction characteristics. *Proceedings of the IRE, 45*(9), 1228-1243.

Sahara, G., & Ishitani, O. (2015). Efficient photocatalysts for CO_2 reduction. *Inorganic chemistry, 54*(11), 5096-5104.

Sasi, S., Rayaroth, M. P., Aravindakumar, C. T., & Aravind, U. K. (2020). Occurrence, distribution and removal of organic micro-pollutants in a low saline water body. *Science of The Total Environment, 749,* 141319.

Serpone, N. (2000). Photocatalysis. Kirk-Othmer *Encyclopedia of Chemical Technology.*

Shang, Y., Fan, H., Chen, Y., Dong, W., & Wang, W. (2022). Synergism between nitrogen vacancies and a unique electrons transfer pathway of Ag modified S-scheme g-C_3N_4/CdS heterojunction for efficient H_2 evolution. *Journal of Alloys and Compounds,* 167620.

Sharma, S., & Bhattacharya, A. (2017). Drinking water contamination and treatment techniques. *Applied Water Science, 7*(3), 1043-1067.

Shawky, A., & Mohamed, R. (2022). S-scheme heterojunctions: emerging designed photocatalysts toward green energy and environmental remediation redox reactions. *Journal of Environmental Chemical Engineering,* 108249.

Shen, R., Xie, J., Guo, P., Chen, L., Chen, X., & Li, X. (2018). Bridging the g-C_3N_4 nanosheets and robust CuS cocatalysts by metallic acetylene black interface mediators for active and durable photocatalytic H_2 production. *ACS Applied Energy Materials*, *1*(5), 2232-2241.

Sudhaik, A., Raizada, P., Khan, A. A. P., Singh, A., & Singh, P. (2022). Graphitic carbon nitride-based upconversion photocatalyst for hydrogen production and water purification. *Nanofabrication, 7.*

Sudhaik, A., Raizada, P., Thakur, S., Saini, A. K., Singh, P., & Hosseini-Bandegharaei, A. (2020). Metal-free photo-activation of peroxymonosulfate using graphene supported graphitic carbon nitride for enhancing photocatalytic activity. *Materials Letters, 277,* 128277.

Sun, J.-X., Yuan, Y.-P., Qiu, L.-G., Jiang, X., Xie, A.-J., Shen, Y.-H., & Zhu, J.-F. (2012). Fabrication of composite photocatalyst gC_3N_4-ZnO and enhancement of photocatalytic activity under visible light. *Dalton Transactions, 41*(22), 6756-6763.

Tahir, M. B., Nabi, G., Rafique, M., & Khalid, N. (2017). Nanostructured-based WO_3 photocatalysts: recent development, activity enhancement, perspectives and applications for wastewater treatment. International Journal of *Environmental Science and Technology, 14*(11), 2519-2542.

Tang, H., Li, R., Fan, X., Xu, Y., Lin, H., & Zhang, H. (2022). A novel S-scheme heterojunction in spent battery-derived $ZnFe_2O_4$/g-C_3N_4 photocatalyst for enhancing peroxymonosulfate activation and visible light degradation of organic pollutant. *Journal of Environmental Chemical Engineering, 10*(3), 107797.

Thornton, J. W., McCally, M., & Houlihan, J. (2002). Biomonitoring of industrial pollutants: health and policy implications of the chemical body burden. *Public Health Reports, 117*(4), 315.

Tkaczyk, A., Mitrowska, K., & Posyniak, A. (2020). Synthetic organic dyes as contaminants of the aquatic environment and their implications for ecosystems: *A review. Science of The Total Environment, 717,* 137222.

Tung, R. T. (2001). Recent advances in Schottky barrier concepts. *Materials Science and Engineering: R: Reports, 35*(1-3), 1-138.

Van, K. N., Huu, H. T., Thi, V. N. N., Le, T.-L. T., Hoang, Q. D., Dinh, Q. V., Vo, V., & Vasseghian, Y. (2022). Construction of S-scheme CdS/g-C_3N_4 nanocomposite with improved visible-light photocatalytic degradation of methylene blue. *Environmental Research, 206,* 112556.

Vedula, R. K., Dalal, S., & Majumder, C. (2013). Bioremoval of cyanide and phenol from industrial wastewater: an update. *Bioremediation Journal, 17*(4), 278-293.

Vieno, N., & Sillanpää, M. (2014). Fate of diclofenac in municipal wastewater treatment plant – A review. *Environment international, 69,* 28-39.

Vinesh, V., Ashokkumar, M., & Neppolian, B. (2020). rGO supported self-assembly of 2D nano sheet of (g-C_3N_4) into rod-like nano structure and its application in sonophotocatalytic degradation of an antibiotic. *Ultrasonics Sonochemistry, 68,* 105218.

Wammer, K. H., Korte, A. R., Lundeen, R. A., Sundberg, J. E., McNeill, K., & Arnold, W. A. (2013). Direct photochemistry of three fluoroquinolone antibacterials: norfloxacin, ofloxacin, and enrofloxacin. *Water Research, 47*(1), 439-448.

Wang, D., Yin, F.-X., Cheng, B., Xia, Y., Yu, J.-G., & Ho, W.-K. (2021). Enhanced photocatalytic activity and mechanism of CeO_2 hollow spheres for tetracycline degradation. *Rare Metals, 40*(9), 2369-2380.

Wang, H., Zhang, L., Chen, Z., Hu, J., Li, S., Wang, Z., Liu, J., & Wang, X. (2014). Semiconductor heterojunction photocatalysts: design, construction, and photocatalytic performances. *Chemical Society Reviews, 43*(15), 5234-5244.

Wang, J., Sun, Y., Fu, L., Sun, Z., Ou, M., Zhao, S., Chen, Y., Yu, F., & Wu, Y. (2020). A defective gC_3N_4/RGO/TiO_2 composite from hydrogen treatment for enhanced visible-light photocatalytic H 2 production. *Nanoscale, 12*(43), 22030-22035.

Wang, J., Wang, G., Cheng, B., Yu, J., & Fan, J. (2021). Sulfur-doped g-C_3N_4/TiO_2 S-scheme heterojunction photocatalyst for Congo Red photodegradation. *Chinese Journal of Catalysis, 42*(1), 56-68.

Wang, J., & Wang, S. (2016). Removal of pharmaceuticals and personal care products (PPCPs) from wastewater: a review. *Journal of Environmental Management, 182,* 620-640.

Wang, J., Wang, Z., Huang, B., Ma, Y., Liu, Y., Qin, X., Zhang, X., & Dai, Y. (2012). Oxygen vacancy induced band-gap narrowing and enhanced visible light photocatalytic activity of ZnO. *ACS Applied Materials & Interfaces, 4*(8), 4024-4030.

Wang, K., Feng, X., Shangguan, Y., Wu, X., & Chen, H. (2022). Selective CO_2 photoreduction to CH_4 mediated by dimension-matched 2D/2D Bi_3NbO_7/g-C_3N_4 S-scheme heterojunction. *Chinese Journal of Catalysis, 43*(2), 246-254.

Wang, L., Cheng, B., Zhang, L., & Yu, J. (2021). In situ irradiated XPS investigation on S-scheme TiO_2@ $ZnIn_2S_4$ Photocatalyst for efficient Photocatalytic CO_2 reduction. *Small, 17*(41), 2103447.

Wang, S., Huang, C.-Y., Pan, L., Chen, Y., Zhang, X., & Zou, J.-J. (2019). Controllable fabrication of homogeneous ZnO pn junction with enhanced charge separation for efficient photocatalysis. *Catalysis Today, 335*, 151-159.

Wang, S., Li, D., Sun, C., Yang, S., Guan, Y., & He, H. (2014). Synthesis and characterization of g-C_3N_4/Ag_3VO_4 composites with significantly enhanced visible-light photocatalytic activity for triphenylmethane dye degradation. *Applied Catalysis B: Environmental, 144*, 885-892.

Wang, W., Zhao, W., Zhang, H., Dou, X., & Shi, H. (2021). 2D/2D step-scheme α-Fe_2O_3/Bi_2WO_6 photocatalyst with efficient charge transfer for enhanced photo-Fenton catalytic activity. *Chinese Journal of Catalysis, 42*(1), 97-106.

Wang, X., Maeda, K., Thomas, A., Takanabe, K., Xin, G., Carlsson, J. M., Domen, K., & Antonietti, M. (2009). A metal-free polymeric photocatalyst for hydrogen production from water under visible light. *Nature Materials, 8*(1), 76-80.

Wang, X., Sayed, M., Ruzimuradov, O., Zhang, J., Fan, Y., Li, X., Bai, X., & Low, J. (2022). A review of step-scheme photocatalysts. *Applied Materials Today, 29*, 101609.

Wang, Y., Wang, Q., Zhan, X., Wang, F., Safdar, M., & He, J. (2013). Visible light driven type II heterostructures and their enhanced photocatalysis properties: a review. *Nanoscale, 5*(18), 8326-8339.

Wei, C., Zhang, W., Wang, X., Li, A., Guo, J., & Liu, B. (2021). MOF-derived mesoporous g-C_3N_4/TiO_2 heterojunction with enhanced photocatalytic activity. *Catalysis Letters, 151*(7), 1961-1975.

Wen, J., Xie, J., Chen, X., & Li, X. (2017). A review on g-C_3N_4-based photocatalysts. *Applied Surface Science, 391*, 72-123.

Wu, F., Li, X., Liu, W., & Zhang, S. (2017). Highly enhanced photocatalytic degradation of methylene blue over the indirect all-solid-state Z-scheme g-C_3N_4-RGO-TiO_2 nanoheterojunctions. *Applied Surface Science, 405*, 60-70.

Wu, J., Huang, Y., Ye, W., & Li, Y. (2017). CO_2 reduction: from the electrochemical to photochemical approach. *Advanced Science, 4*(11), 1700194.

Wu, Y., Meng, D., Guo, Q., Gao, D., & Wang, L. (2022). Study on TiO_2/g-C_3N_4 S-Scheme heterojunction photocatalyst for enhanced formaldehyde decomposition. *Optical Materials, 126*, 112213.

Xia, C., Huang, H., Liang, D., Xie, Y., Kong, F., Yang, Q., Fu, J., Dou, Z., Zhang, Q., & Meng, Z. (2022). Adsorption of tetracycline hydrochloride on layered double hydroxide loaded carbon nanotubes and site energy distribution analysis. *Chemical Engineering Journal, 443*, 136398.

Xiao, C., Wang, L., Zhou, Q., & Huang, X. (2020). Hazards of bisphenol A (BPA) exposure: A systematic review of plant toxicology studies. *Journal of Hazardous Materials, 384*, 121488.

Xiao, J., Liu, X., Pan, L., Shi, C., Zhang, X., & Zou, J.-J. (2020). Heterogeneous photocatalytic organic transformation reactions using conjugated polymers-based materials. *ACS Catalysis, 10*(20), 12256-12283.

Xu, H., Wu, L., Jin, L., & Wu, K. (2017). Combination mechanism and enhanced visible-light photocatalytic activity and stability of CdS/g-C_3N_4 heterojunctions. *Journal of Materials Science & Technology, 33*(1), 30-38.

Xu, J., Wang, W., Sun, S., & Wang, L. (2012). Enhancing visible-light-induced photocatalytic activity by coupling with wide-band-gap semiconductor: A case study on Bi_2WO_6/TiO_2. *Applied Catalysis B: Environmental, 111*, 126-132.

Xu, L., Zhang, H., Xiong, P., Zhu, Q., Liao, C., & Jiang, G. (2021). Occurrence, fate, and risk assessment of typical tetracycline antibiotics in the aquatic environment: *A review. Science of The Total Environment, 753*, 141975.

Xu, Q., Zhang, L., Cheng, B., Fan, J., & Yu, J. (2020). S-scheme heterojunction photocatalyst. *Chem, 6*(7), 1543-1559.

Xu, T., Liang, J., Li, S., Xu, Z., Yue, L., Li, T., Luo, Y., Liu, Q., Shi, X., & Asiri, A. M. (2021). Recent advances in nonprecious metal oxide electrocatalysts and photocatalysts for N_2 reduction reaction under ambient condition. *Small Science, 1*(5), 2000069.

Yan, S., Li, Z., & Zou, Z. (2009). Photodegradation performance of g-C_3N_4 fabricated by directly heating melamine. *Langmuir, 25*(17), 10397-10401.

Yang, J., Zhang, X., Xie, C., Long, J., Wang, Y., Wei, L., & Yang, X. (2021). Preparation of g-C_3N_4 with high specific surface area and photocatalytic stability. *Journal of Electronic Materials*, *50*(3), 1067-1074.

Yang, K., Zhang, H., Liu, T., Xiang, D., Li, Y., & Jin, Z. (2022). Tailoring of efficient electron-extracting system: S-scheme g-C_3N_4/$CoTiO_3$ heterojunction modified with Co_3O_4 quantum dots for photocatalytic hydrogen evolution. *Journal of Electroanalytical Chemistry*, 922, 116749.

Yang, X., Hesami, M. D., Nazemipool, E., Bahadoran, A., Al-Bahrani, M., & Azizi, B. (2022). Fabrication of $CuCo_2S_4$ yolk-shell spheres embedded with S-scheme V_2O_5-deposited on wrinkled g-C_3N_4 for effective promotion of levofloxacin photodegradation. Separation and Purification Technology, 301, 122005.

Yang, X., Tian, L., Zhao, X., Tang, H., Liu, Q., & Li, G. (2019). Interfacial optimization of g-C_3N_4-based Z-scheme heterojunction toward synergistic enhancement of solar-driven photocatalytic oxygen evolution. *Applied Catalysis B: Environmental*, *244*, 240-249.

Yang, Y., Liu, Z., Demeestere, K., & Van Hulle, S. (2021). Ozonation in view of micropollutant removal from biologically treated landfill leachate: Removal efficiency, OH exposure, and surrogate-based monitoring. *Chemical Engineering Journal*, *410*, 128413.

Yu, J., Wang, S., Low, J., & Xiao, W. (2013). Enhanced photocatalytic performance of direct Z-scheme gC_3N_4-TiO_2 photocatalysts for the decomposition of formaldehyde in air. Physical *Chemistry Chemical Physics*, *15*(39), 16883-16890.

Yuan, F., Zheng, Y., Gao, D., Wang, L., & Hu, X. (2022). Facile assembly and enhanced visible-light-driven photocatalytic activity of S-scheme BiOBr/g-C_3N_4 heterojunction for degrading xanthate in wastewater. *Journal of Molecular Liquids*, *366*, 120279.

Yuan, Y., Guo, R.-t., Hong, L.-f., Lin, Z.-d., Ji, X.-y., & Pan, W.-g. (2022). Fabrication of a dual S-scheme $Bi_7O_9I_3$/g-C_3N_4/Bi_3O_4Cl heterojunction with enhanced visible-light-driven performance for phenol degradation. *Chemosphere*, *287*, 132241.

Zhang, B., Shi, H., Yan, Y., Liu, C., Hu, X., Liu, E., & Fan, J. (2021). A novel S-scheme 1D/2D Bi_2S_3/g-C_3N_4 heterojunctions with enhanced H_2 evolution activity. *Colloids and Surfaces A: Physicochemical and Engineering Aspects*, *608*, 125598.

Zhang, C., Jia, M., Xu, Z., Xiong, W., Yang, Z., Cao, J., Peng, H., Xu, H., Xiang, Y., & Jing, Y. (2022). Constructing 2D/2D N-ZnO/g-C_3N_4 S-scheme heterojunction: efficient photocatalytic performance for norfloxacin degradation. *Chemical Engineering Journal*, *430*, 132652.

Zhang, G., Xue, Y., Wang, Q., Wang, P., Yao, H., Zhang, W., Zhao, J., & Li, Y. (2019). Photocatalytic oxidation of norfloxacin by $Zn_{0.9}Fe_{0.1}S$ supported on Ni-foam under visible light irradiation. *Chemosphere*, *230*, 406-415.

Zhang, L., Zhang, J., Yu, H., & Yu, J. (2022). Emerging S-scheme photocatalyst. Advanced Materials, 34(11), 2107668.

Zhang, M., Yang, Y., An, X., & Hou, L.-a. (2021). A critical review of g-C_3N_4-based photocatalytic membrane for water purification. *Chemical Engineering Journal*, 412, 128663.

Zhang, Q., Bai, X., Hu, X., Fan, J., & Liu, E. (2022). Efficient photocatalytic H_2 evolution over 2D/2D S-scheme $NiTe_2$/g-C_3N_4 heterojunction with superhydrophilic surface. *Applied Surface Science*, *579*, 152224.

Zhang, S., Fan, Q., Xia, R., & Meyer, T. J. (2020). CO_2 reduction: from homogeneous to heterogeneous electrocatalysis. *Accounts of chemical research*, *53*(1), 255-264.

Zhang, W., Mohamed, A. R., & Ong, W. J. (2020). Z-Scheme photocatalytic systems for carbon dioxide reduction: where are we now? *Angewandte Chemie International Edition*, *59*(51), 22894-22915.

Zheng, D., Pang, C., & Wang, X. (2015). The function-led design of Z-scheme photocatalytic systems based on hollow carbon nitride semiconductors. *Chemical Communications*, *51*(98), 17467-17470.

Zhou, P., Yu, J., & Jaroniec, M. (2014). All-solid-state Z-scheme photocatalytic systems. *Advanced Materials*, *26*(29), 4920-4935.

Zhou, Y., Wang, Z., Huang, L., Zaman, S., Lei, K., Yue, T., Li, Z. a., You, B., & Xia, B. Y. (2021). Engineering 2D photocatalysts toward carbon dioxide reduction. *Advanced Energy Materials*, *11*(8), 2003159.

Zhu, B., Xia, P., Li, Y., Ho, W., & Yu, J. (2017). Fabrication and photocatalytic activity enhanced mechanism of direct Z-scheme g-C_3N_4/Ag_2WO_4 photocatalyst. *Applied Surface Science*, *391*, 175-183.

Zhu, B., Zhang, L., Cheng, B., Yu, Y., & Yu, J. (2021). H_2O molecule adsorption on s-triazine-based g-C_3N_4. *Chinese journal of catalysis*, *42*(1), 115-122.

Zhu, Q., Xu, Z., Qiu, B., Xing, M., & Zhang, J. (2021). Emerging cocatalysts on g-C_3N_4 for photocatalytic hydrogen evolution. *Small*, *17*(40), 2101070.

Zhu, X., Wang, Y., Guo, Y., Wan, J., Yan, Y., Zhou, Y., & Sun, C. (2021). Environmental-friendly synthesis of heterojunction photocatalysts g-C_3N_4/$BiPO_4$ with enhanced photocatalytic performance. *Applied Surface Science*, *544*, 148872.